Optimization of a RF Single Ion Paul Trap for a $^{88}Sr^{+}$ Ion Optical Clock Comparison

by

Maria Tibbo

Thesis submitted to the
Faculty of Graduate and Postdoctoral Studies
In partial fulfillment of the requirements
For the M.Sc. degree in
Graduate Program in Physics

Physics
Faculty of Science
University of Ottawa

"All we have to decide is what to do with the time that is given us." - Gandalf

J.R.R Tolkien, The Fellowship of the Ring

Abstract

As part of the ongoing world-wide effort in improving time and frequency references, a high accuracy optical frequency standard was developed using the electric quadrupole allowed $5s\ ^2S_{1/2} \rightarrow 4d\ ^2D_{5/2}$ clock transition at 445 THz (674 nm) in a trapped and laser cooled $^{88}Sr^+$ ion. An ion trap system of the endcap design has been recently evaluated with a fractional frequency uncertainty which surpasses the accuracy of the current realization of the SI second. This thesis seeks to further evaluate the limiting systematic shifts of the device by optimizing a second ion trap reference based on a rf Paul trap design, which was then compared with the endcap trap reference frequency. The comparison of the two ion traps' reference frequencies confirmed an overall offset of -0.36 $\pm$ 0.08 Hz at the 445 THz reference frequency corresponding to a fractional frequency offset of 8×10^{-16}.

Acknowledgements

I would like to thank Pierre Dubé whose patience and help was instrumental to both the experimental and theoretical work in this project. Thanks to Andre Diamant Boustead the summer student. Mostly, thanks to my supervisor Alan Madej for his wise guidance and generous allocation of his time that was essential to the timely completion of this thesis and my future in science.

Contents

List of Figures

List of Tables

1 Introduction

Time maintains a central role in physics as it provides a foundation for physical measurements of nature. The creation of an accurate and precise unit of time, the second, is critical as it is an essential unit in science. The accuracy and stability of a standard for time and frequency establishes the ultimate limitations on measuring the unit. The second is unique in that it is the most accurately realized fundamental unit measured with exceptional precision allowing the evaluation of fundamental constants and concepts in physics [8]. A precise definition of a second is also imperative as it is a foundation for other standards of basic units including the meter, ampere, and candela.

The second was originally defined as a fraction of the mean solar day, but this definition was inaccurate due to the irregularities in the rotation of the Earth. To improve the accuracy of the definition, the second was then redefined as a fraction of the time it takes for Earth to orbit the sun referenced to the year 1900. However, with the inaccuracies of astronomy still present in the definition, and experiments confirming that an atomic standard involving a transition between energy levels in atoms was much more precise and reproducible, the International Conference on Weights and Measures (CGPM) defined the SI unit of a second in 1967 as [8]:

The duration of 9 192 631 770 periods of the radiation corresponding to the transition between the two hyperfine levels of the ground state of the cesium 133 atom.

Defining a precision atom-based frequency standard impacts directly on the performance of realizing the second and allowed orders of magnitude improvement in the ability to probe changes in the physical universe using clocks. A clock basically consists of a stable oscillator and a counter to count the number of oscillations. In order for the clock to provide a

stable frequency, the oscillator must be referenced to a frequency discriminator to prevent drifting. In theory, any regular oscillator in nature could serve as a base for timekeeping, however atoms were recognized as the ideal frequency reference due to their immunity to environmental forces, and high reproducibility [9]. In the present work, an optical atomic clock uses extremely stable and narrow-band laser radiation as an oscillator used to excite a transition in an atom which acts as a frequency discriminator. Since atoms only absorb frequencies that match their natural energy levels, the probe laser is referenced to this exact frequency.

Microwave atomic clocks based on cesium have achieved fractional frequency uncertainties of 2×10^{-16} [10], however optical frequency standards based on narrow linewidth transitions in trapped atoms offer increased stability and accuracy beyond the cesium reference standard. In particular, the environment created by suspending single, trapped, atomic ions and probing the atomic system on long lived, dipole forbidden transitions has provided the best experimental realizations to date for an atomic system with the lowest level of evaluated uncertainty. Progress has been made worldwide in frequency standards based on transitions in Ba^+ [5], Sr^+ [11], Ca^+ [12], Hg^+ [9], In^+ [13], Yb^+ [14], and Al^+ [15].

The Frequency and Time group within the Measurements Science and Standards Portfolio at the National Research Council of Canada (NRC) has developed a high accuracy optical frequency standard using the electric quadrupole allowed $5s\ ^2S_{1/2} \rightarrow 4d\ ^2D_{5/2}$ clock transition at 445 THz (674 nm) in a trapped and laser cooled $^{88}Sr^+$ ion. The natural linewidth of this transition is 0.4 Hz, resulting in a line with a potential quality factor of $Q = 1 \times 10^{15}$.

The initial $^{88}Sr^+$ ion reference system was based on a rf Paul trap to suspend the single atomic ion being studied [11]. After several advances in the fields of ion trap design, precision measurements, and optics, the NRC team developed a next generation ion trap of the endcap design [3, 16]. The new endcap ion trap system was recently evaluated to reach a fractional uncertainty of 2.3×10^{-17} [3], surpassing the accuracy, by an order of magnitude, of the current realization of the SI second obtained from a Cs atomic clock. Using the endcap ion trap, the frequency of the $^{88}Sr^+$ ion $S-D$ clock transition was measured by comparison with a maser system referenced to the SI second, currently responsible for the realization of time in Canada. The measured frequency was 444 779 044 095 485.5(9) Hz [3].

1.1 Project Outline

The purpose of this work was to conduct a high accuracy optical frequency comparison of the two optical clocks. The use of two optical systems allows the realization of high precision results in much shorter averaging times than can be achieved if the optical clock system is compared to a traditional radio frequency standard. In addition, the lower systematic uncertainties associated with the optical clock system allow the investigation of shifts and uncertainties at levels beyond that obtainable with rf frequency/time standards. The current work involves simultaneously observing the $^{88}Sr^{+}$ ion $S - D$ clock transition in the older rf Paul trap and the new endcap trap, then measuring the frequency difference. To achieve this goal, this thesis project involved several modifications to the older rf Paul trap system to effectively reduce the shifts and uncertainties of the ion trap from the last calculated fractional frequency uncertainty of 3.4×10^{-14} reported in 2005 [17]. These improvements include upgrading the laser system used to excite and cool the single ion transition, the optimization of Gaussian beam optics, and addition of piezo-electric driven motor mounts on mirrors for precision control of beam position. In order to quantify critical ion parameters causing frequency shifts, several studies were performed including mass spectroscopy to determine collisional rates, measurements of parameters effecting the ion temperature, the minimization of micromotion, as well as a careful investigation of laser power and detuning for optimal use of the five different radiations used in the trap experiment.

These studies and modifications increased precision control and reliability of factors contributing to the containment of the ion in the rf Paul trap and control of the ion in the trap environment. The enhancement of the rf Paul trap system had a great impact on the frequency comparison with the endcap trap as the length of ion holding time in the rf Paul trap is generally the limiting factor in the experiment. In order to achieve measurement uncertainties that are approaching the evaluated systematic shift limits, measurement averaging times on the order of hours to days are necessary. The improvements made in this work allowed the possibility for such measurements.

Similar world-class level frequency difference experiments have been performed in previous work including an optical clock comparison of two $^{88}Sr^{+}$ ion rf Paul traps at the National Physical Laboratory (NPL) in the United Kingdom in 1999 achieving a fractional difference of 3×10^{-13} [18]. In 2012, NPL accomplished another comparison of two $^{88}Sr^{+}$ ion endcap

traps obtaining a fractional difference of 3×10^{-16} [19]. As well, optical clock comparisons of other previously mentioned ion systems have been reported. Two trapped $^{171}Yb^{+}$ ion systems at Physikalisch-Technische Bundesanstalt (PTB) in Germany in 2005, obtained a fractional difference of 3.8×10^{-16} [14]. In 2010, The National Institute of Standards and Technology (NIST) reported a fractional frequency difference of 1.8×10^{-17} via comparison of two quantum logic Al^{+} ion optical clocks [15].

The goal of the project is to complete a frequency difference comparison between the two optical clocks, and obtain results comparable to previous work. The recent developments of this work will contribute to a better evaluation of the limiting systematic shifts and uncertainties on the single ion system. It will also lay the groundwork for a future gravitational time dilation measurement of the two optical clocks placed at different heights.

2 Theory

2.1 Fundamental Concepts of Ion Trapping and Confinement

The use of an ion trap system allows one to approach the ideal condition of a well localized, isolated atomic particle that is nearly free of external perturbation such as collisions with the containment vessel and stray field gradients. Moreover, the conditions encountered in an ion trap environment provide a significant reduction in complications of the atom−light interaction by removing such problems as the transit of the atom across the optical beam, elimination of the first-order Doppler shift when the ion is localized at length scales below the wavelength of light used to probe the transition [20, 21], and reductions in the second-order Doppler shifts (relativistic time dilation) due to the relative motion of the ion and the laboratory. An additional advantage using an ion trap is the ability to store a single ion for an extended period of time thus allowing a continuous sequence of measurements performed on the same atomic absorber.

The rf quadrupole Paul trap consists of three electrodes: two endcap electrodes situated a distance of $2z_o$ apart, and a ring electrode of diameter $2r_o$ positioned symmetrically between the endcap electrodes, see Figure 2.1 [2]. The geometry of this electrode setup creates a parabolic potential well when a potential is applied to the electrodes. However, Earnshaw's theorem [22] states that a particle cannot be maintained in a stable equilibrium configuration purely by interaction with electrostatic forces of other charges. The solution is to apply a sinusoidal time varying potential to the electrodes at time scales shorter than the ion's mean transit time across the trap structure. Solving the equation of motion over many cycles of the time varying potential yields bound motion of the ion moving in an equivalent pseudo potential of a three dimensional harmonic well [23].

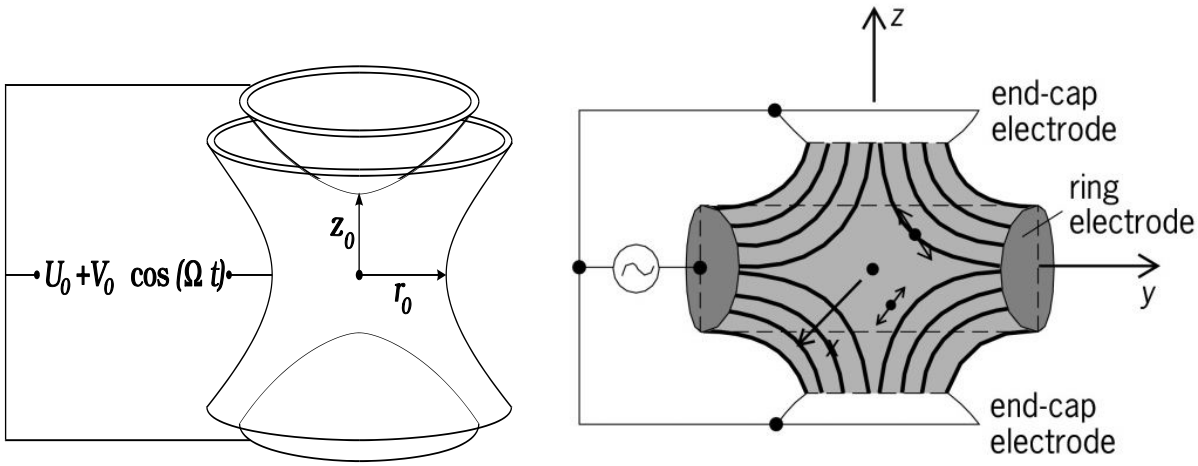

Figure 2.1: Diagram of a rf Paul trap and the ion's oscillation amplitude for different locations in the trap (from Ref. [1, 2]).

The quadrupole potential in the trap can be expressed as [24]:

$$\phi(r,z,t) = \frac{\phi_o(t)}{r_o^2 + 2z_o^2}(r^2 - 2z^2) \tag{2.1}$$

$$\phi_o(t) = U_o + V_o \cos(\Omega t) \tag{2.2}$$

where U_o is a static potential amplitude, V_o is the time varying trapping potential amplitude applied with the trap drive oscillation frequency $f = \Omega/2\pi$, r_o is the distance from the trap center to the ring electrode along the radial direction (r), and z_o is the distance of an endcap electrode from the center of the trap along the axial direction (z). The strength of the radial and axial potential can be defined along these orthogonal directions. When the trap is not perfectly symmetrical, the radial confinement potential can be described by x

and y axes. Invariably, imperfections in the trap potential symmetry results in a breakdown in the radial degeneracy resulting two approximately equal, but different, radial potential directions. The kinetic energy of the ion motion coupled with the time averaged trap potential results in an oscillatory motion described by secular frequencies. These secular frequencies are for motion along the radial and axial axes and are proportional to the depth of the trapping potential along the respective axis. In the case of the rf Paul trap used in this project, the static potential applied between the endcap and ring electrodes was usually set to zero. With $U_o = 0$, the axial, ω_z, and the radial, $\omega_r \approx \omega_x \approx \omega_y$, angular secular frequencies can be expressed as [23, 25]:

$$\omega_z = 2\omega_r = \frac{q\Omega}{2\sqrt{2}} \tag{2.3}$$

$$q = \frac{8eV_o}{m\Omega^2(r_o^2 + 2z_o^2)} \tag{2.4}$$

where q is a parameter characterizing the trap stability, e the charge of an electron, and m the ion mass. The motion of the ion in the trap can be described by a Mathieu differential equation, where the q parameter characterizing boundary conditions for the ion's stable confinement [23]. In the case of positive values of U_o, increasing values of U_o will decrease the axial secular frequency and increase the radial secular frequencies. In practice, observation of spectral features at these secular frequencies away from the reference spectral line are used to calculate the $^{88}Sr^+$ ion's temperature in the trap [26].

For ions with no dissipative force, the conservation of energy in the trap potential keeps externally injected charged particles from remaining in the three dimensional harmonic well. This means the trap must be loaded with neutral atoms provided by a small oven [27], and then photoionized once near the center of the trap [28].

2.2 $^{88}Sr^+$ Ion

An ion used as an optical frequency reference requires a clock transition with a long lived upper state yielding a narrow natural linewidth that is relatively insensitive to perturbations. In order to reduce the ion's motion in a trap, the atomic system of choice should possess a strongly allowed transition between the ground and an upper state, so that the

ion can rapidly absorb and re-emit photons enabling Doppler laser cooling and emit copious amounts of fluorescence for detection. The frequencies required to excite these transitions, as well as the transitions involved in the ionization a neutral atom, should all be easily obtained with commercial laser sources. The $^{88}Sr^{+}$ ion was chosen as a frequency reference because it satisfies the trapping, laser cooling, and optical reference transition conditions.

2.2.1 Energy Levels

Figure 2.2 is an energy level diagram of the $^{88}Sr^{+}$ ion. Radiation at the 422 nm transition wavelength excites the dipole allowed transition $5s\ ^2S_{1/2} - 5p\ ^2P_{1/2}$ that has an upper state lifetime of $\tau = 7.35(30)$ ns [29]. Since this transition has a very short lifetime and strong dipole moment, it can scatter more than 10^7 photons per second under proper excitation, making it suitable for both fluorescence detection and Doppler laser cooling.

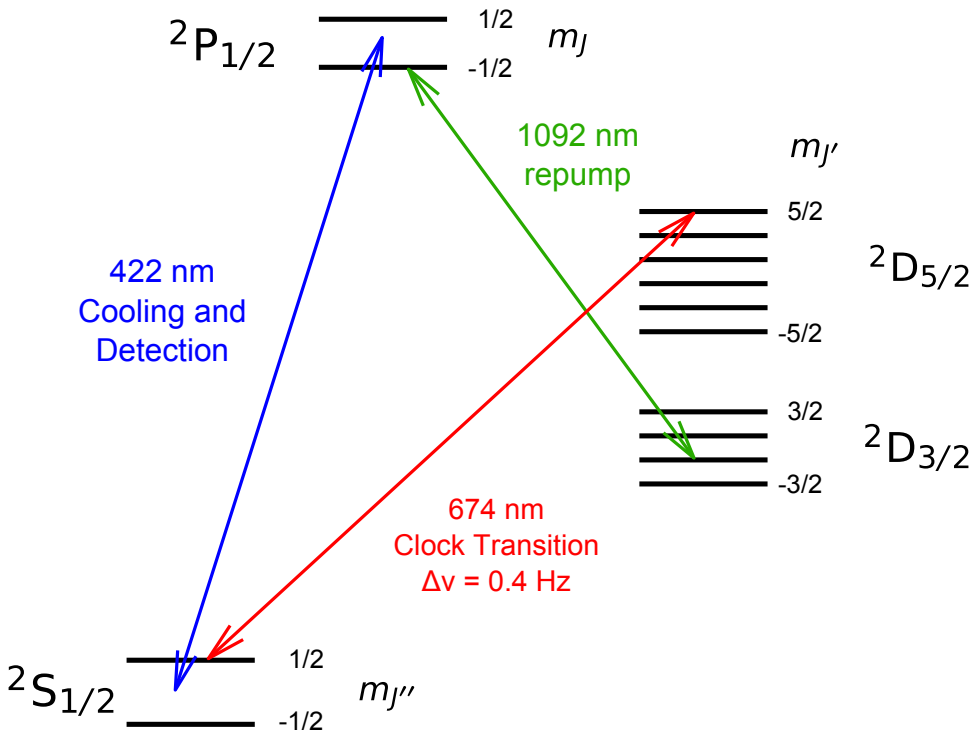

Figure 2.2: Partial energy level diagram for the $^{88}Sr^{+}$system showing the three relevant transitions (from Ref. [3]).

Doppler laser cooling is a method of using optical radiation to reduce the trapped ion's kinetic motion. The ion is essentially invisible to all non-resonant frequencies except when a laser is tuned to an allowed transition frequency of the atomic system. Here, the ion absorbs the photon's energy and momentum, and then re-emits a photon in a random direction. When the laser frequency is detuned slightly lower from resonance and the ion is moving towards the propagating beam of photons, the ion sees photons frequency shifted towards the resonance transition due to the Doppler effect. The ion preferentially absorbs the photons of this detuned energy and re-emits photons at the same energy in the ion's frame of reference. The photon's appear, on average, to be at higher energy in the lab frame due to the Doppler effect. The increase in net emitted energy is obtained from the kinetic energy of the ion and therefore there is a reduction in the ion's motional energy. This process is repeated until the ion is successfully laser cooled to an equilibrium value [30]. For optimum laser cooling, the 422 nm laser is typically red detuned to the half intensity point of the natural linewidth for the strongly allowed $S - P$ transition of the trapped $^{88}Sr^{+}$ ion. Typical kinetic temperatures achieved with Doppler cooling result in values on the mK level; with the limit of such processes for the $S - P$ transition being 0.5 mK [31].

The $^{2}P_{1/2}$ state has a 1:13 branching ratio to the metastable $^{2}D_{3/2}$ state that possesses a long natural lifetime. The ion cannot be laser cooled when the electron is shelved in this state, therefore 1092 nm radiation is necessary to repump the electron back to the upper state so cooling and detection can resume.

The clock transition is the an electric quadrupole allowed $5s\,^{2}S_{1/2}-4d\,^{2}D_{5/2}$ transition excited by 674 nm radiation. The upper state has a long natural lifetime of $\tau = 390.8(1.6)$ ms [32], giving a natural linewidth of $\Delta\nu = 0.4$ Hz and quality factor of $Q = \nu/\Delta\nu = 10^{15}$.

The $^{88}Sr^{+}$ ion is exposed to a magnetic field inside the trap, and the Zeeman effect causes the degenerate levels of the $5s\,^{2}S_{1/2}-4d\,^{2}D_{5/2}$ transition to separate. The Zeeman splitting creates two ground state levels and six excited state levels, and a transition can be excited between any pair that follows the quadrupole selection rule $\Delta m = 0, \pm 1, \pm 2$. The energy shift in each transition due to the Zeeman splitting is given by:

$$h\Delta\nu = \mu_B B(g_j' m_j' - g_j'' m_j'') \tag{2.5}$$

where h is Planck's constant, μ_B is the Bohr magneton, m_j'' and m_j' are the magnetic quantum numbers for the ground state level and excited state level respectively, B is the

magnetic flux density of the magnetic field, $\Delta\nu$ is the transition frequency shift, and g_j is the Landé factor. The Landé factors were determined in previous work as [33]:

$$g_{1/2} = 2.002319 \tag{2.6}$$

$$g_{5/2} = 1.200385 \tag{2.7}$$

The frequency shifts of the Zeeman components, $\Delta\nu$, for both ion trap systems used in the current studies are obtained experimentally using a frequency scan of the probe laser. The shift rate and observed background field splittings in the two experimental systems are given in Table 2.1. It was determined that the average background magnetic fields were approximately 3.4 μT and 2.0 μT based upon the spectral scans in the rf Paul trap and endcap trap respectively.

Table 2.1: RF Paul Trap and Endcap Trap Zeeman Shifts

Zeeman Component	Ground State m_j''	Excited State m_j'	Zeeman Shift (kHz/μT)	Zeeman Shift RF Paul Trap $\Delta\nu$ (kHz)	Zeeman Shift End Cap Trap $\Delta\nu$ (kHz)
$\pm$C1	$\mp 1/2$	$\mp 1/2$	± 5.6124	± 18.75	± 11.30
$\pm$C2	$\pm 1/2$	$\pm 3/2$	± 11.190	± 37.75	± 22.70
$\pm$C3	$\mp 1/2$	$\pm 1/2$	± 22.415	± 75.25	± 45.30
$\pm$C4	$\pm 1/2$	$\pm 5/2$	± 27.992	± 94.25	± 56.30
$\pm$C5	$\mp 1/2$	$\pm 3/2$	± 39.217	± 132.00	± 79.30

2.2.2 Photoionization

The photoionizing scheme used in the trap loading process to convert a neutral strontium atom to a $^{88}Sr^{+}$ ion is shown in the schematic diagram in Figure 2.3 [4]. The ionization is produced via a two step process. The first step uses 461 nm radiation for the $5s^2\ ^1S_0$ - $5s5p\ ^1P_1$ resonance line transition. The second step excites the atom with 405 nm radiation to the autoionizing $4d^2\ ^1D_2$ resonance where the electron is freed and the atom is now a $^{88}Sr^{+}$ ion. Using this two laser source arrangement, efficient ionization of the incident loaded atoms into the trap can occur resulting in low deposition of material on the trap structure and avoiding the creation of spurious stray patch potentials and fields.

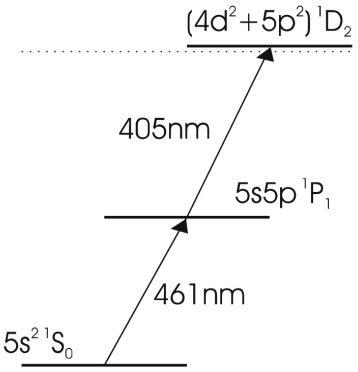

Figure 2.3: Photoionization process of a $^{88}Sr^{+}$ ion (from Ref. [4]).

2.3 Frequency Line Center Determination

As previously stated, the $^{88}Sr^{+}$ ion is exposed to a background magnetic field inside the trap, and the $5s\ ^2S_{1/2} - 4d\ ^2D_{5/2}$ transition is separated into 10 Zeeman components shifted symmetrically around the zero field line center. The probe laser can be tuned to excite the transition between these components. During probing, the dominant effect defining spatial quantization of the atom's angular momentum is provided by the residual background magnetic field. This then defines the axis of quantization of the system. In general, the relative strengths of the Zeeman component transitions are a function of the incident beam direction relative to the quantization axis (defined by the background magnetic field) and the light polarization [33]. An example of a particular series of line intensities and frequency splitting between the components can be seen in Figure 2.4.

Measurement of the linecentre is performed by detuning the probe laser to a pair of Zeeman components located symmetrically about the linecentre. In this experiment, the laser frequency is detuned by passing a fixed laser frequency through an acousto-optic modulator

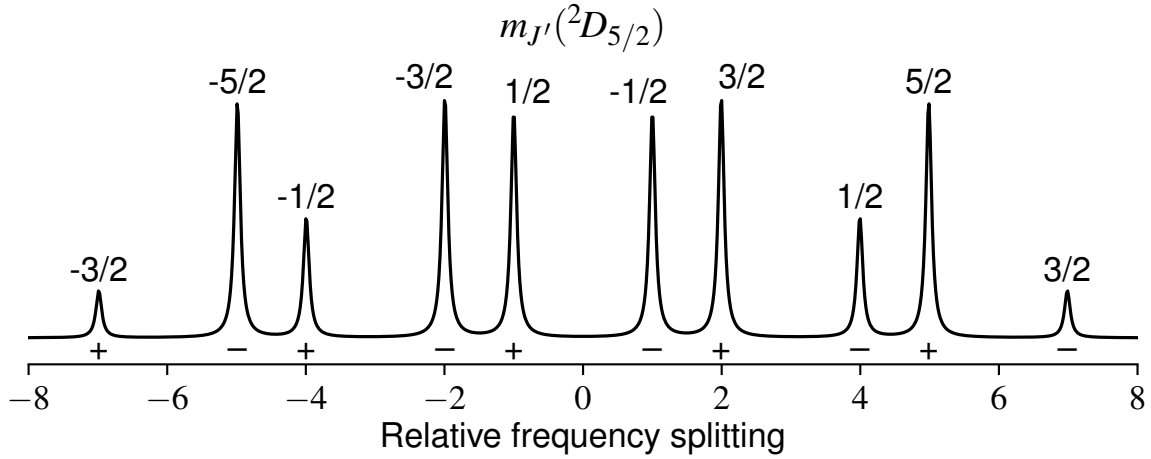

Figure 2.4: Relative frequency splitting of the Zeeman components of the clock transition. The fraction above the transition denotes the upper state value of m_j and the + and - symbols below the component indicate the lower state +1/2 and -1/2 m_j states involved (from Ref. [3]).

(AOM). Such a device can precisely detune the laser output with an rf frequency offset that can be accurately generated using a computer controlled frequency synthesizer. The AOM shifted 674 nm probe laser frequency then is stabilized to a pair of Zeeman components, equally spaced from the zero-field linecenter. For each component, the transition rate is measured at the two frequencies separated by the component's linewidth, indicated with red circles in Figure 2.5. By determining the AOM frequencies that balance the transition rate on both sides, the center frequency of each component can be calculated by averaging these two frequencies. The linear Zeeman shift is removed by averaging the component frequencies to find the center frequency [34], indicated with a large red arrow in Figure 2.5.

This measurement cycle is then repeated for another pair of Zeeman components. The center frequencies of the Zeeman pairs are then averaged in a way that cancels different sensitivities of each component pair to other undesired frequency shifts. One such shift is the electric quadrupole shift caused by the interaction of the upper level of the clock transition with the electric field gradient of the trap. A more detailed explanation of this calculation is given in [17]. The resulting mean frequency is the AOM offset frequency that corresponds to the field free clock transition line center [34]. Knowledge of the absolute frequency of the fixed laser source together with the AOM frequency then can be used to determine the absolute frequency of the field free clock transition.

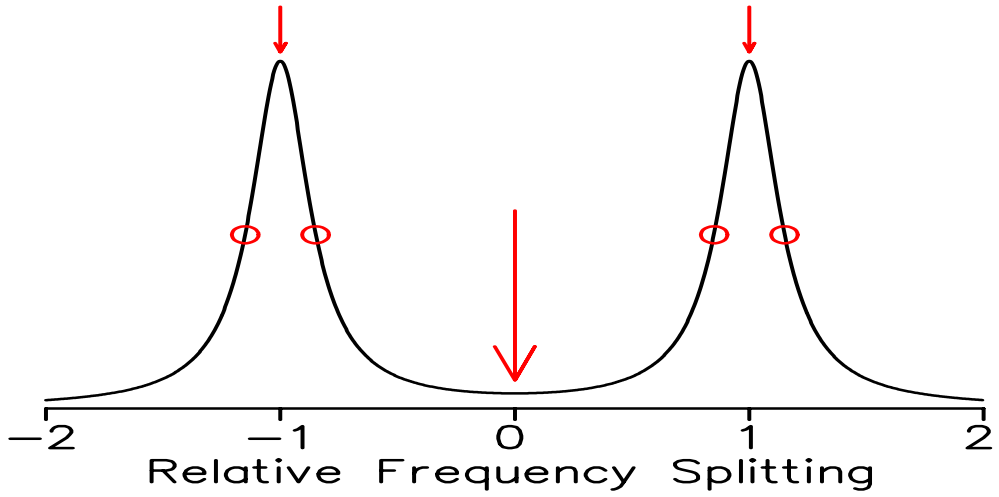

Figure 2.5: A schematic drawing of the inner Zeeman components pair spectrum, ±C1 is shown. Locking points (shown as red circles) on the red and blue sides of each component are used to average for the center frequency of each component (shown by the small red arrows). The component frequencies are then averaged to find the center frequency of the transition (large red arrow) (from Ref. [3]).

2.4 Micromotion and the 'Magic' Frequency

In the ideal case, the $^{88}Sr^{+}$ ion would be positioned in the center of the trap, where the trapping field amplitudes disappear. However, in reality, imperfections in the trap, stray fields and other effects result which cause ion to undergo micromotion driven by the ac electric field at the applied frequency $\frac{\Omega}{2\pi}$ of the trap [35]. Micromotion can be caused by inadequacies in the trap such as patch potentials caused by material build up on the electrodes due to loading, a phase difference in the potentials applied to the electrodes, and the ion's residual kinetic energy. It is essential to successfully minimize micromotion in both ion traps, otherwise large frequency shifts result.

The micromotion frequency shifts induce a Stark effect and second-order Doppler effect on the unperturbed transition. The shifts are both strongly correlated to the applied frequency of electric field that drives the micromotion. The micromotion also results in a first order Doppler effect on the Zeeman component frequency spectrum of the S-D transition, creating sidebands at the trap frequency $\frac{\Omega}{2\pi}$ [35]. Previous work [3] determined a specific 'magic' trap drive frequency where the Stark shift and the second order Doppler shift cancel, greatly reducing micromotion associated perturbations. A brief summary of the calculation of the 'magic' frequency is given.

Only the scalar Stark shift is relevant in this calculation, as the tensor Stark shift is cancelled in the averaging method used to remove the quadrupole shift mentioned in the previous section. The fractional scalar Stark shift for the S-D transition of the $^{88}Sr^{+}$ ion is expressed as [3]:

$$\frac{\Delta\nu_{Stark}}{\nu_0} = -\frac{\Delta a_0}{\hbar\omega_0}\left(\frac{m\Omega^2 c}{e\omega_0}\right)^2 \sum_{x,y,z} R_i \tag{2.8}$$

where $\nu_0 = \frac{\omega_0}{2\pi}$ is the clock transition frequency, $\Delta\alpha_0$ is the difference in the polarizabilites of the $D_{5/2}$ and $S_{1/2}$ levels, m is the mass of the ion, e is the charge of the ion, c is the speed of light, and R_i is an experimentally measured micromotion sideband to carrier transition intensity ratio along a particular probed direction $i = x, y, z$. The fractional second order Doppler shift can be expressed as:

$$\frac{\Delta\nu_{D2}}{\nu_0} = -\left(\frac{\Omega}{\omega_0}\right)^2 \sum_{x,y,z} R_i \tag{2.9}$$

Combining these two micromotion shifts gives:

$$\frac{\Delta\nu_{\mu}}{\nu_0} = -\left(\frac{\Omega}{\omega_0}\right)^2 \left[1 + \frac{\Delta a_0}{\hbar\omega_0}\left(\frac{m\Omega c}{e}\right)^2\right] \sum_{x,y,z} R_i \tag{2.10}$$

It can be seen that for $\Delta\alpha_0$ having negative values, a choice of the trap operating frequency Ω can be made such that the term in the square brackets can vanish. Using the best known value of $\Delta\alpha_0 = -4.83(17) \times 10^{-40}$ J m^2/V^2 [36], $\Delta\nu_{\mu}$ vanishes when the scalar Stark shift and second order Doppler shifts are equal in value and opposite in sign. This occurs when the trap frequency equals:

$$\frac{\Omega}{2\pi} = \frac{e}{2\pi mc}\sqrt{-\frac{\hbar\omega_0}{\Delta a_0}} = 14.39(25) \text{ MHz} \tag{2.11}$$

This is the 'magic' trap frequency value that was used in the measurements described in this work.

3 Experimental Setup

3.1 The RF Paul Trap

The fundamental concepts of ion trapping in a rf Paul trap were summarized in Section 2.1. In this work, the rf Paul trap has an endcap electrode to trap center distance of z_o= 0.5 mm with a ring electrode to trap center distance of r_o=$\sqrt{2} \times z_o$= 0.71 mm. A schematic cross section diagram of the electrode configuration of the rf Paul trap is seen in Figure 3.1 [11]. Tantalum was chosen as the material for the electrode components due to its low out gassing properties in ultra-high vacuum environments and its ability to be easily spot welded to the support structures holding the trap. In these experiments, a trapping voltage of about 720 V peak to peak amplitude is applied between the endcap and ring electrodes at the trap drive 'magic' frequency. The trap parameters are listed in Table 3.1. This results in radial secular frequencies of $\nu_x,\ \nu_y \approx 900$ kHz, and an axial secular frequency of $\nu_z \approx 1800$ kHz.

Table 3.1: Parameters for rf Paul Trap

Trap Parameter	Value
z_0	0.5 mm
r_0	0.71 mm
$\frac{\Omega}{2\pi}$	14.39 MHz
V_0	360 V
U_0	0 V

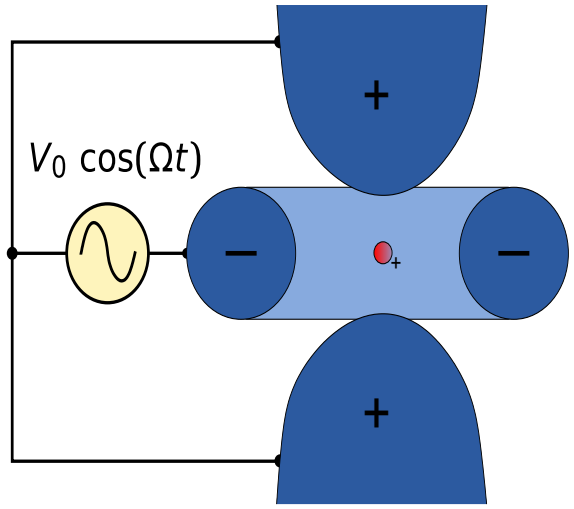

Figure 3.1: A cross section diagram of the rf Paul trap electrode configuration with two endcap electrodes and a ring electrode. Lengths of electrodes shown are not to scale.

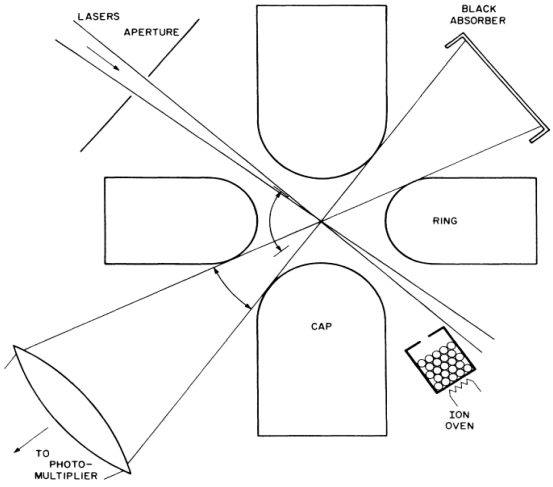

Figure 3.2: Cross section diagram of the rf Paul trapping apparatus with laser beam entry, oven, and fluorescence collection (from Ref. [5]).

The ion trap apparatus is located inside a ultra-high vacuum (UHV) chamber evacuated by an ion pump system to the 80 nPa level. The trap is loaded by photoionizing neutral Sr atoms that are emitted out of a small oven containing a $SrAl_4$ and Ni powder mixture [27]. Once the trap is successfully loaded with a single $^{88}Sr^+$ ion, the photoionizing beams are turned off. The 422 nm ion fluorescence signal is observed and recorded with a photomultiplier tube (PMT). The 422 nm fluorescence is collected outside the vacuum chamber with a large numerical aperture lens (NA = 2), sending the collimated light through a narrow bandpass filter centered at 421.7 nm and having a transmission of over 0.95 [Iridian Spectral Technologies]. This filter effectively suppresses any scattered radiation from the other laser wavelengths. The light is then focused with a second matching lens onto a 100 μm diameter pinhole located in front of the PMT. In order to maximize the fluorescence-background ratio the pinhole position was optimized by centering it with micrometer screws onto the ion image. Figure 3.2 [5] is a diagram of the trapping electrodes relative to ion oven, the angle of the incident laser beams and the light cone for fluorescence detection. The total efficiency of the system including light collection solid angle, filter losses, and photomultiplier sensitivity is estimated to be 4×10^{-3}.

Figure 3.3: The rf Paul trap optical table with the optical set up required for all five laser radiations. The magnetic shield is shown covering the ion trap vacuum apparatus, and the recently added focusing lens system with two pico-tilt translator mirrors are located immediately before the magnetic shield entrance aperture.

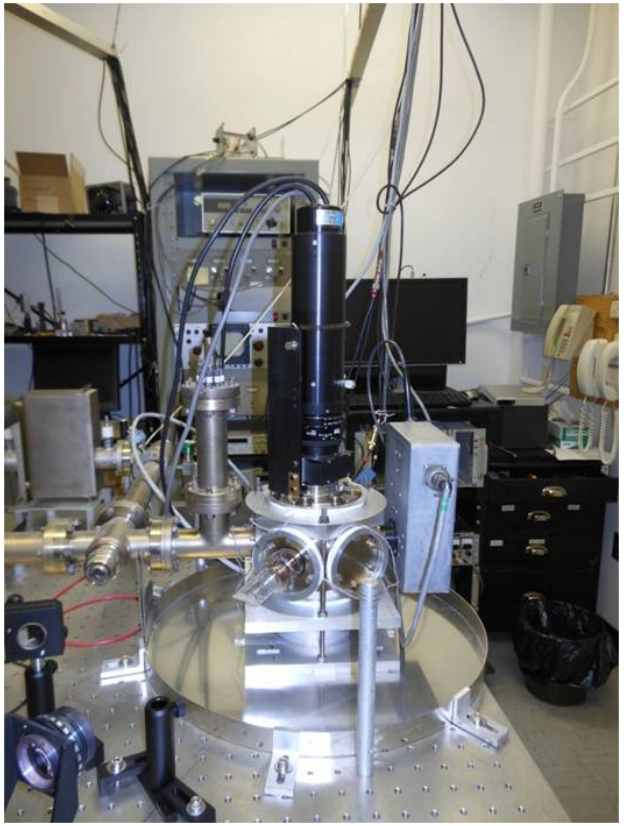

Figure 3.4: The rf Paul trap vacuum enclosure with the magnetic shield removed, providing a view of the photomultiplier tube housing and the Brewster windows designed to minimize scattering of the laser radiation going into the trap.

3.2 The Endcap Trap

Several advances were made in the field of ion trap design, precision measurement and optics, which resulted in the construction at NRC of an improved next generation ion trap of the endcap design. The same basic principles of the rf Paul trap apply to the newer endcap trap, however the electrode structure has been altered to increase laser beam accessibility to the trapped $^{88}Sr^{+}$ ion. If an ion were to be confined in between just two endcap electrodes stray ac and dc fields could perturb the confining electric field between the electrodes. Although a ring electrode successfully protects against these fields, it blocks easy access along the x-y plane for laser beams and other optics used for detection. Instead, the endcap design uses two concentric shield electrodes held at ground potential and located around the endcap electrode wires. The shield electrode-trap center distance is comparable to the endcap separation, and therefore alters the electric field providing the same effect as the ring electrode, but with free access along three orthogonal laser beams axes [16].

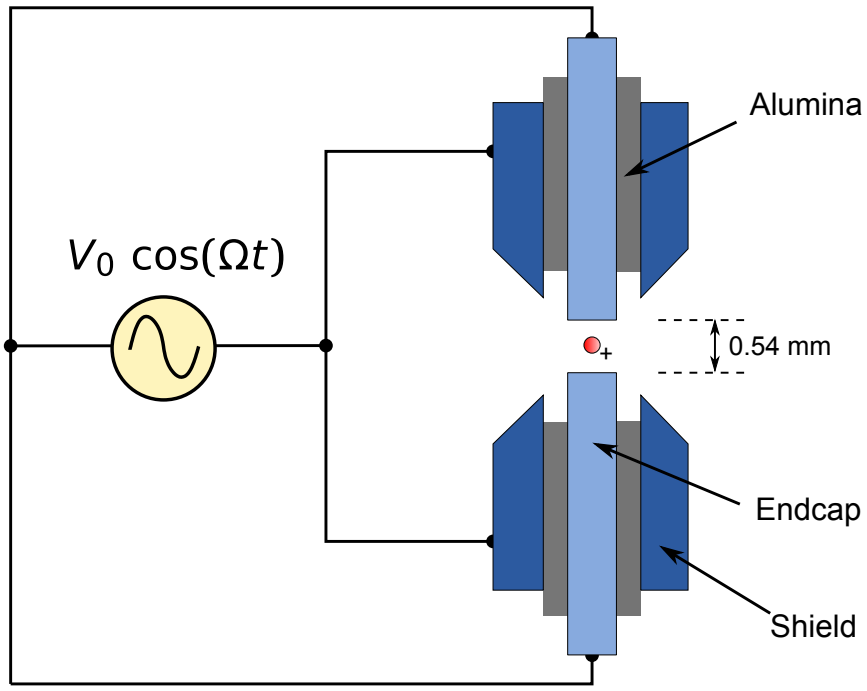

Figure 3.5: A cross section depiction of the endcap trap electrode configuration where shield electrodes located around the main rf drive electrodes have replaced the ring electrode used in the rf Paul trap. Lengths of electrodes shown are not to scale (from Ref. [3])

The electrode configuration of the endcap design is seen in Figure 3.5. The trapping apparatus consists of endcap electrodes made with molybdenum wires, enclosed by tantalum tubes functioning as shield electrodes. Alumina tubes are situated between the endcap and shield electrodes to provide electrical insulation. A DC bias potential applied to the endcap electrodes allows control of the ion position along the axial direction, while two orthogonal trim electrodes, located about 5 mm from the trap center, control the ion position along the radial direction. A trapping voltage of about 426 V peak-to-peak is applied between the endcap and shield electrodes at the 'magic' frequency of 14.39 MHz. This results in radial secular frequencies of $\nu_x,\ \nu_y \approx 1200$ kHz, and an axial secular frequency of $\nu_z \approx 2300$ kHz.

The trap is located inside a vacuum chamber with ports providing access for the three orthogonal laser beam axes, a UHV ion pump, the photomultiplier tube, and a charge-coupled device (CCD) camera. The CCD camera is positioned opposite to the PMT port, and is used to observe the ion motion and displacement in a plane perpendicular to the PMT CCD camera axis [3]. The camera employs the same narrow-bandpass filter as the PMT as well as an extra filter for the 1092 nm radiation. The CCD optical system has a total magnification of 13.5×, with a resolution limit of about 3 pixels, $\approx 3\ \mu$m [3]. The photon counting photomultiplier system has similar characteristics as described for the rf trap apparatus but incorporates a higher numerical aperture aspheric lens (NA$\approx$ 0.5) mounted inside the vacuum chamber for higher collection efficiency.

Table 3.2: Parameters for Endcap Trap

Trap Parameter	Value
z_0	0.27 mm
$\frac{\Omega}{2\pi}$	14.39 MHz
V_0	213 V
U_0	0 V

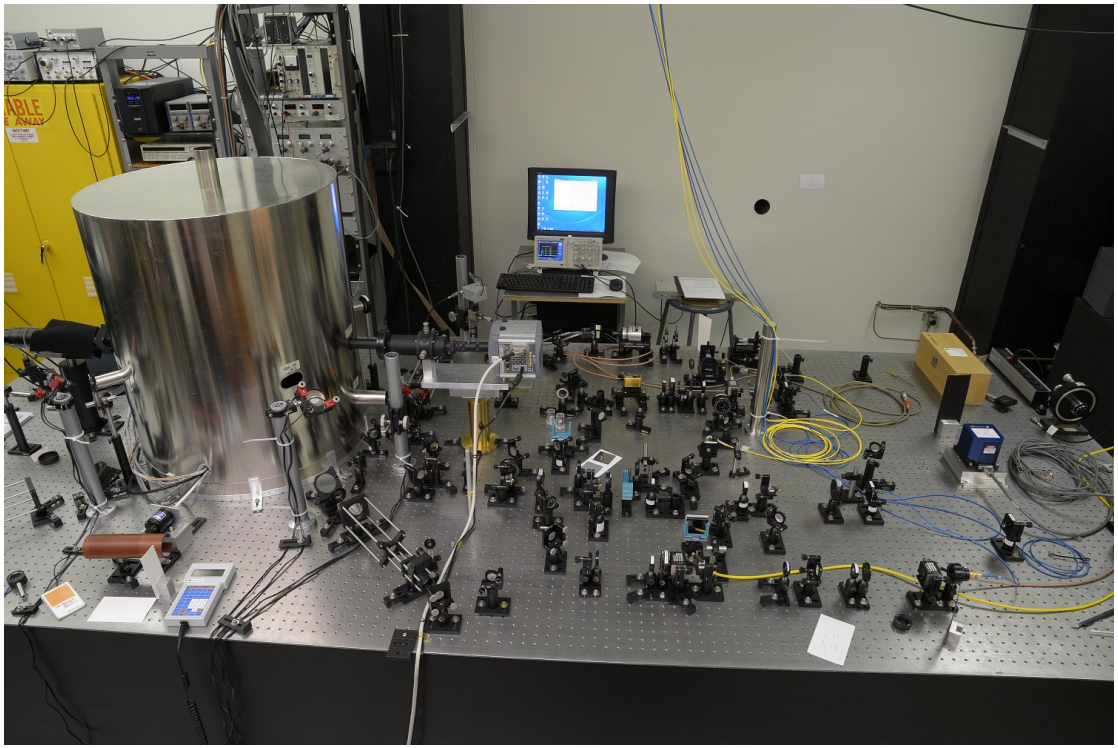

Figure 3.6: The NRC endcap trap optical table with the optical set up required for all five laser radiations. Here there are three entrances into the trap magnetic shield, all have a lens focusing system and two pico-tilt translator mirrors prior to the entrances providing precision control along 3 axes. The CCD camera is located as the grey device near the centre of the photo (photo courtesy of P. Dubé).

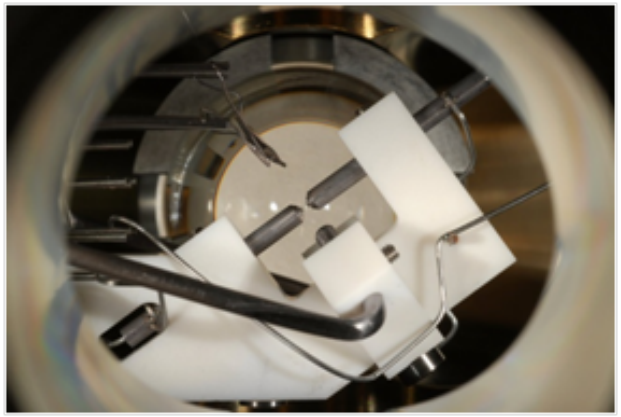

Figure 3.7: Photograph of the endcap electrodes inside the vacuum enclosure. The Sr oven source can be seen above the endcap trap and one dc radial trim electrode is seen in the foreground (photo courtesy of P. Dubé).

3.3 Laser Systems

Each trap setup uses its own free running diode laser (405 nm) for the second step ionization of the Sr neutral sent into the trap. This is due to the high optical losses encountered with the propagation of the short wavelength 405 nm radiation via optical fiber. The other laser systems used in this experiment including the first step ionization (461 nm), repump (1092 nm), probe (674 nm), and cooling and detection (422 nm) sources, were built prior to this current work and are provided to each ion trap via optical fibers. A brief summary of each laser system is given in this section.

3.3.1 Setup of the First Step Ionization Laser System

A frequency doubled diode laser produces the 461 nm radiation used for the first step of the ionization process. It operates at $\lambda = 460.862$ nm for the $^1S_0 - {}^1P_1$ resonance line transition of the Sr neutral atoms, with a maximum power output of 170-200 mW. This beam is used in both ion trap experiments. The 461 nm laser system is based on a master laser, tapered amplifier, and a second-harmonic generation (SHG) unit. The master laser is an external cavity diode operated at 922 nm providing output power at the mW level. The tapered amplifier amplifies the master laser and outputs a beam of about 500 mW which is then used as the fundamental beam for the SHG unit. The SHG unit (converting a portion of the 922 nm radiation to 461 nm) consists of a build-up cavity that increases the optical pump power for the periodically poled $LiNbO_3$ nonlinear crystal used for the frequency conversion. A Hänsch-Couillaud (HC) detection method is used to lock the master frequency to resonance frequency in the build-up cavity [37]. The HC locking technique does not require a modulation of the laser frequency or power, instead the error signal is obtained using the change in the ellipticity of the polarization caused by the build-up cavity. More detail on the 461 nm photoionization laser system is given in previous work [38]. Although the laser system is capable of generating a few hundred milliwatts, only a few mW are sent to each ion trap apparatus to prevent damage to the single mode optical fiber being used. Typical incident powers on the ion are at the sub-mW level which is more than sufficient to saturate the neutral transition for ionization.

3.3.2 Setup of the Cooling and Detection Laser System

A key element in the stable, long term storage, laser cooling and fluorescence detection of the ion is the 422 nm laser source. The cooling and detection laser operates at $\lambda = 421.7$ nm for the $5s\ ^2S_{1/2} - 5p\ ^2P_{1/2}$ transition. The 422 nm laser diode is offset locked to a saturated absorption resonance of ^{85}Rb using a double-pass AOM which covers the frequency difference between the Sr^+ and Rb transitions. The 422 nm laser used with a Rb spectrometer is a commercial External Cavity Diode Laser (ECDL) [Toptica DL 100 PRO] that consists of a GaN laser diode and a diffraction grating in Littrow configuration that provides selective frequency feedback to the laser diode. The diffraction grating positions can be changed with a Piezo Electric Actuator (PZT). Radiation from the 422 nm ECDL is directed through two optical isolators, and to a beam splitter where approximately 50% of the laser power is sent to the Rb spectrometer and diagnostic FabryPerot (FP) cavity. The portion of the beam sent to the Rb spectrometer passes through an AOM twice to obtain a net frequency down-shift before the radiation is used in saturated absorption spectroscopy in

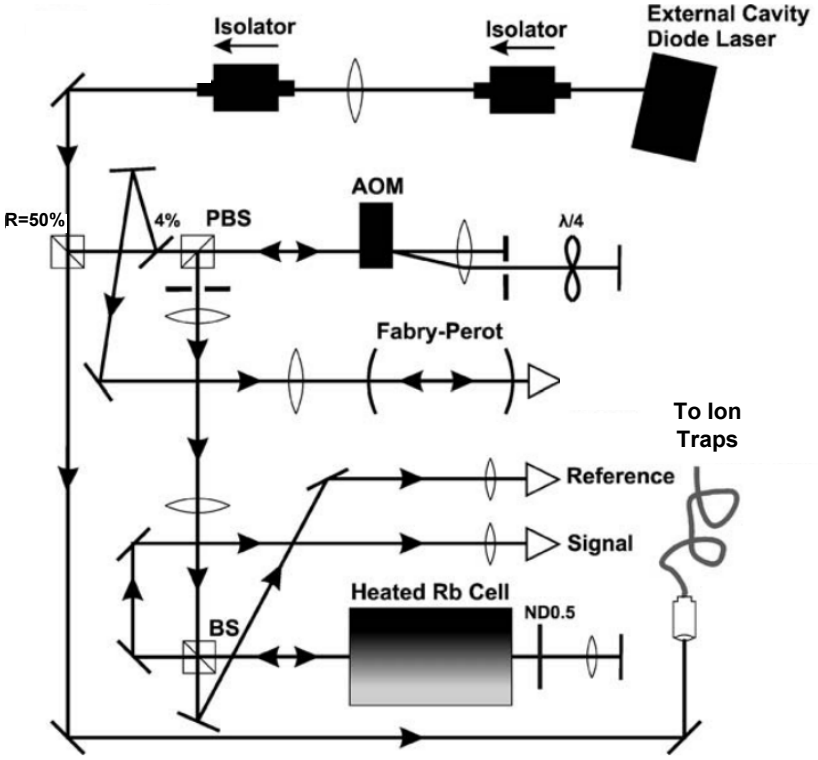

Figure 3.8: Optical layout of the 422 nm laser system with the Rb spectrometer (from Ref. [6]).

the Rb cell to produce a frequency stabilization signal. The rest of the beam is focused into the optical fiber for ion trap use. Tuning of the laser is achieved by changing the frequency of the AOM thus changing the frequency offset of the unshifted laser beam relative to the reference Rb absorption line [6].

Optimal laser cooling is obtained by slight red detuning of the 422 nm frequency from the $S-P$ cooling transition linecenter. A diagram of the original setup for the 422 nm laser system is given in Figure 3.8. More details of the cooling laser system set can be found in previous work [6].

As previously stated the laser system was already implemented, however this work did involve replacing the 422 nm diode laser. The original 422 nm laser had low power and a tendency to unlock periodically (due to mode hopping). Different characteristics of a

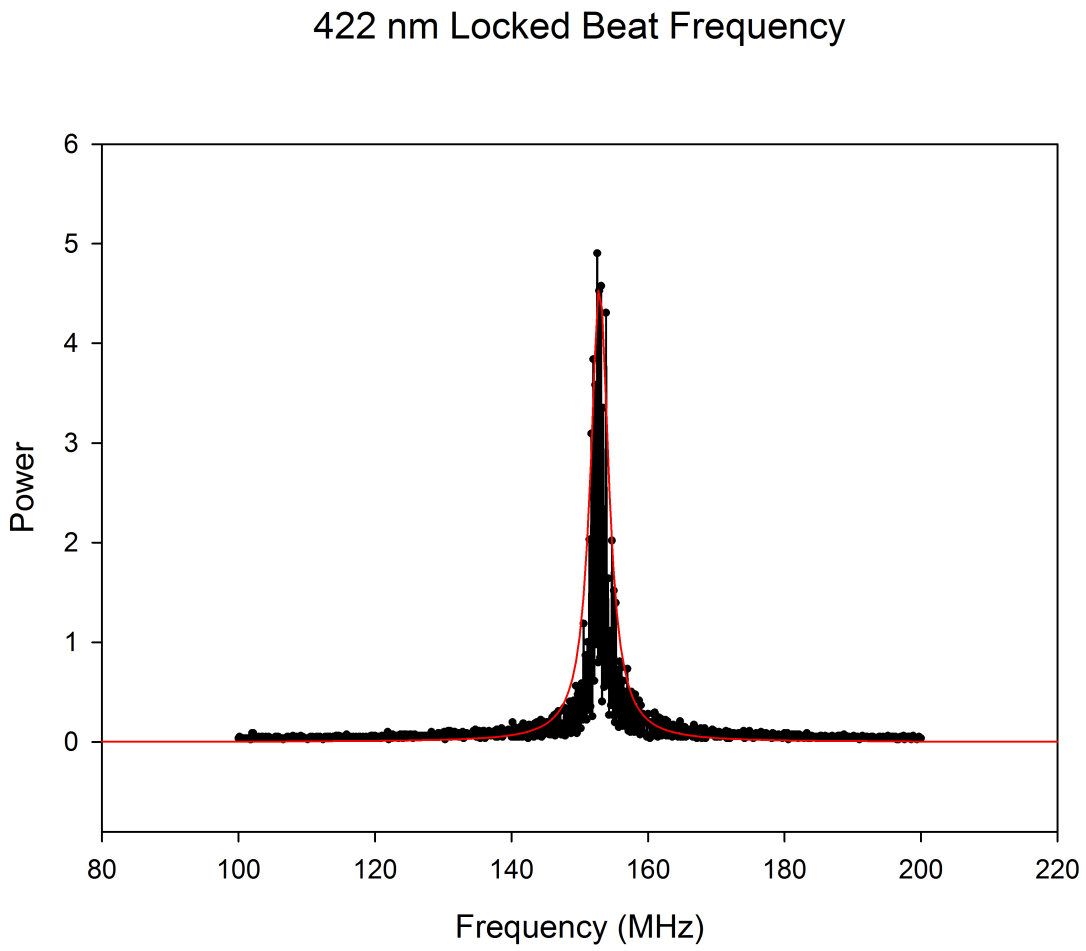

Figure 3.9: Beat Frequency of the Old and New 422 nm Lasers, FWHM: 3.3 MHz

new 422 nm laser were investigated to ensure the replacement increased the long term stability and reliability of the source. As shown in Figure 3.9 the heterodyne frequency beat between the new and old laser sources resulted in a full width at half maximum (FWHM) beat frequency linewidth of 3.3 MHz. Based on previous studies of the original laser which determined its linewidth to be 2 MHz, it was determined that the new laser had a smaller linewidth and was less prone to mode hopping due to improved cavity design and temperature stability.

In order to optimally install the new 422 nm diode, the beam was characterized to determine the transverse shape of the beam as well as its Gaussian beam parameters. The parameters for optimal coupling into the fiber were determined and then adjusted experimentally for maximum power through the fiber. The new 422 nm laser was installed and coupled into the fiber for use in both ions traps. This new cooling and detecting laser has since proven to stay locked for extended periods of time of about 8 days, and is no longer a limiting factor in the experiment. Typical powers sent to each ion trap apparatus were ≈ 100 μW with P= 1 to 5 μW directed to the ion.

3.3.3 Setup of the Repump Laser System

The repump laser is a commercial diode-pumped fiber laser [Koheras Adjustik Y10] operated at 1092 nm for the $4d\ ^2D_{3/2} - 5p\ ^2P_{1/2}$ transition. The laser uses Ytterbium-doped fiber with a mirror and a fiber Bragg grating as cavity reflectors. The wavelength can be controlled coarsely, with a mode-hop free tuning range of 90 GHz, using the laser unit's temperature control. Direct tuning and control is achieved by a PZT stretching element applied to the fiber. Applying a voltage of 0 V - 150 V to the fiber provides a fine wavelength control of about 3 GHz. The single mode frequency of the laser is stabilized to a reference polarization-stabilized helium-neon laser using a transfer Fabry-Perot cavity. This stabilization method provides continuous locking and operation for the repump laser use in both ion traps. An AOM is used in both traps for chopping the light of the repump beam before entering the ion trap. More detail of the 1092 nm repump beam and its stabilization can be found in previous work [39]. Incident powers of a few 100 μW are available at each ion experiment with powers of ≈ 5 μW sent to the single ion.

3.3.4 Setup of the Probe Laser

A spectrally ultranarrow probe laser is operated at 674 nm for the $5s\ ^2S_{1/2} - 4d\ ^2D_{5/2}$ clock transition. The radiation is provided by an extended-cavity diode laser that is frequency stabilized using the Pound-Drever-Hall (PDH) technique [40] to two subsequent evacuated reference Fabry-Perot (FP) cavities. The final locking cavity has an extremely high finesse (160 000) and is fabricated with ultralow expansion (ULE) glass material. The laser is locked to a longitudinal mode in the FP cavity that produces a frequency close to the clock transition, and the remaining frequency difference is frequency shifted using a double-pass AOM. In order to achieve no frequency drift due to temperature variations, the ULE reference cavity is contained in a vacuum vessel stabilized to the temperature at which the ULE material has a linear thermal expansion coefficient of zero. The probe laser setup allows computer controlled, precision tuning and locking to transition line center frequencies at the Hz level. Results show that this setup has achieved a probe laser linewidth of $\Delta\nu = 4.4(3)$ Hz, seen in Figure 3.11 [3]. A schematic diagram of the 674 nm probe laser system is shown in Figure 3.10. More detail on the set up of this system can be found in previous work [7].

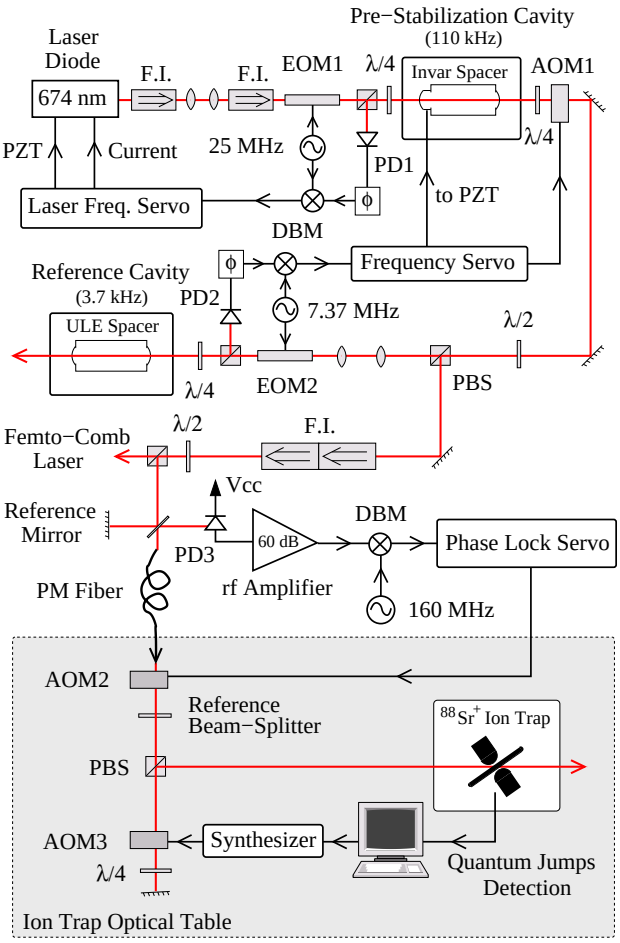

Figure 3.10: Optical layout of the 674 nm probe laser system. The shaded area indicates components located on each ion trap table. From Ref. [7]

The absolute frequency of the radiation probing the ion is the sum of the fixed laser frequency stabilized to the ULE reference cavity together with the frequency shift provided by the tunable AOM driven by a precision frequency synthesizer. Each ion trap system has

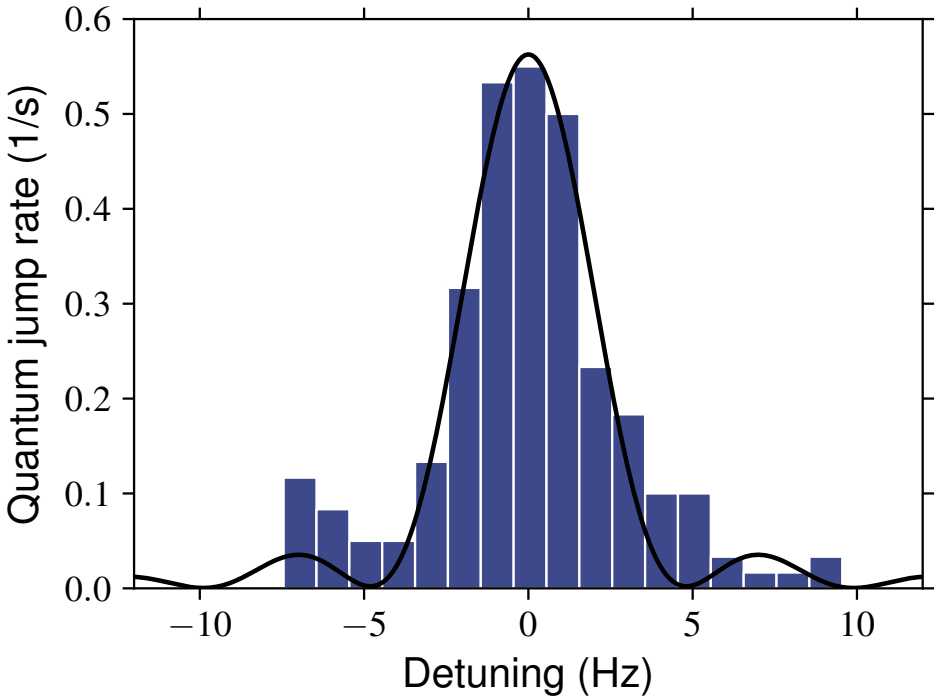

Figure 3.11: High resolution spectrum of a Zeeman component, showing the laser probe linewidth of the 674 nm beam to be $\Delta\nu = 4.4(3)$ Hz. The histogram shows the number of quantum jumps as a function of frequency detuning, and the solid curve is a computation of the fitted Rabi excitation spectrum (from Ref.[3]).

its own AOM and referenced synthesizer used to independently tune the radiation directed into the different ion traps. The ion frequency difference between the two ion traps [3] is thus the difference in the two systems' AOM frequencies recorded. The common ULE stabilized laser frequency drops out of the calculation.

3.4 Cooling-Probing-Detection Cycle

Direct observation of the clock transition in the $^{88}Sr^{+}$ ion via 674 nm fluorescence detection is impractical due to the long natural lifetime of the transition. The ion would radiate a few 674 nm photons per second, and the detection system would only collect a small fraction of the fluorescence. Therefore the clock transition is monitored indirectly using the electron shelving/quantum jump method [30]. The PMT monitors the 422 nm fluorescence of the strong dipole allowed transition, $5s\ ^2S_{1/2} - 5p\ ^2P_{1/2}$. This transition is extremely

short lived (about 7 ns), and scatters more than 10^6 photons/s. However, when the ion is excited on the electric quadrupole allowed $5s\ ^2S_{1/2} - 4d\ ^2D_{5/2}$ clock transition, the electron is 'shelved' in the $4d\ ^2D_{5/2}$ level. During this time the $^{88}Sr^+$ ion is unable to absorb a 422 nm photon, interrupting the millions of 422 nm photons that would be scattered, and a temporary loss in fluorescence (quantum jump), is observed. This sudden drop in fluorescence can easily be detected with near unity quantum efficiency. This electron shelving method is extremely effective in detecting the clock transition of the $^{88}Sr^+$ ion and dipole forbidden transitions in other atomic systems [30].

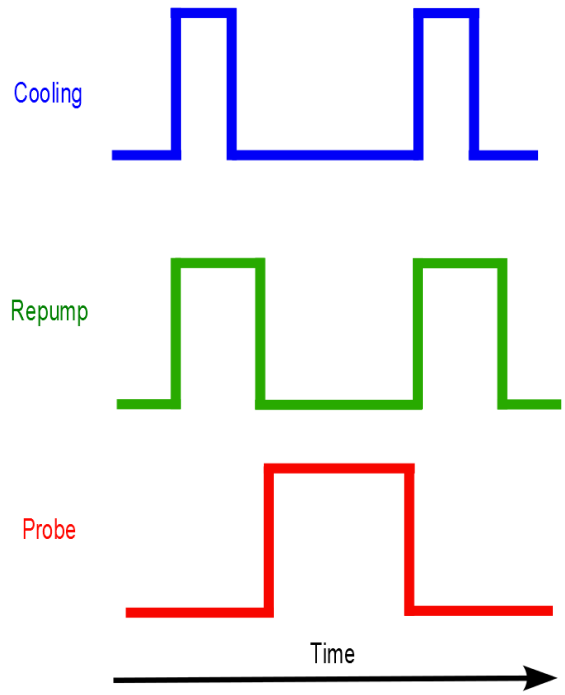

Figure 3.12: Chopper pulse diagram of the cooling, probing, detection cycle. Not to scale.

A specific sequence in excitation of the trapped ion is required for a successful cooling-probing-fluorescence detection cycle. First the ion is cooled with a pulse of the 422 nm beam, as well as the 1092 nm radiation to repump the ion out of the metastable $^2D_{3/2}$ state. The pulse of 1092 nm radiation is slightly longer then the 422 nm pulse, to guarantee any possible $^2D_{3/2}$ state population returns to the ground state. A short buffering time

between the probe pulse, 674 nm radiation, and the cooling pulse, including both the 422 nm and 1092 nm radiations, is required to prevent ac-Stark shifts and ensure the clock transition is not power broadened.

The cooling pulse is about 20 ms long, with an approximate buffering time of 3 ms before the 100 ms probe pulse. The cooling pulse is then used again, this time as a detection tool to see if the probe pulse successfully excited the ion to the $4d\ ^2D_{5/2}$ state. The cooling-probing-detection cycle then repeats. The pulses of radiation are created by blocking the laser radiations with choppers. The 422 nm light is mechanically chopped with a galvomotor actuated aluminium blade before being sent to both ion traps via fiber optic cables. The probe and repump lasers are chopped by AOMs. Figure 3.12 is an approximate timing diagram of the chopper pulse of each radiation for the cooling-probing-detection cycle.

Table 3.3 is a summary of the operational characteristics of the laser systems. It outlines the laser wavelengths, λ, with their beam radius at the ion, w_o, the typical trapping powers, and chopping apparatus. Various studies as described in Sections 4.3 and 4.4 provide justification for the selection of these optimal beam parameters. Note that the 405 nm photoionizing beam is not a well characterized Gaussian beam, and therefore does not have an assigned focussed beam radius, w_o. The focussed beam radii of the 461 nm radiations were also not directly measured in these studies.

Table 3.3: Operating Characteristics of the Laser Systems

λ (nm)	Paul Trap w_o (μm)	Paul Trap Power (μW)	Endcap Trap w_o (μm)	Endcap Trap Power (μW)	Chopping Method
405		250		300	
461		300		300	
422	20(1)	2	16(1)	0.4	Mechanical
1092	54(1)	2	51(2)	4	AOM
674	30(5)	0.000 1	32(5)	0.000 03	AOM

Figure 3.13 summarizes the major components of the laser systems, choppers, photo-multiplier, and computer involved in both the rf Paul trap and the endcap trap systems.

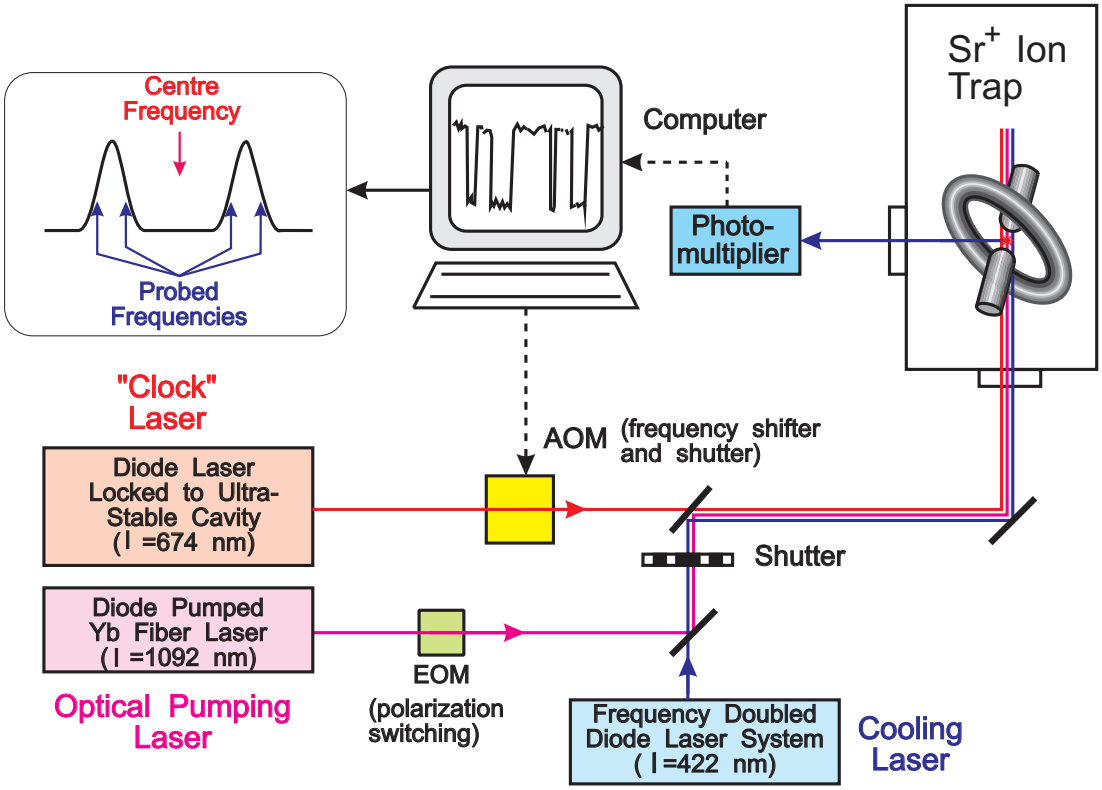

Figure 3.13: Diagram of the major components involved in the ion trapping systems.

3.5 RF Paul Trap Laser Studies, Modifications, and Improvements

3.5.1 First Step Ionization Laser: 461 nm

An important requirement for the effective photoionization of the incident Sr neutral atoms is to have the 461 nm first stage excitation in resonance with the Sr $S - P$ line transition. A study was done to examine the lineshape of the 461 nm radiation interacting with the neutral beam of Sr atoms from the oven. Using the fluorescence provided by the photomultiplier in the rf Paul trap and by continuously loading many ions in the trap, a scan over the detuning of the 461 nm radiation was taken as shown in Figure 3.14. The plot essentially shows the ionization efficiency as a function of detuning. The linewidth was

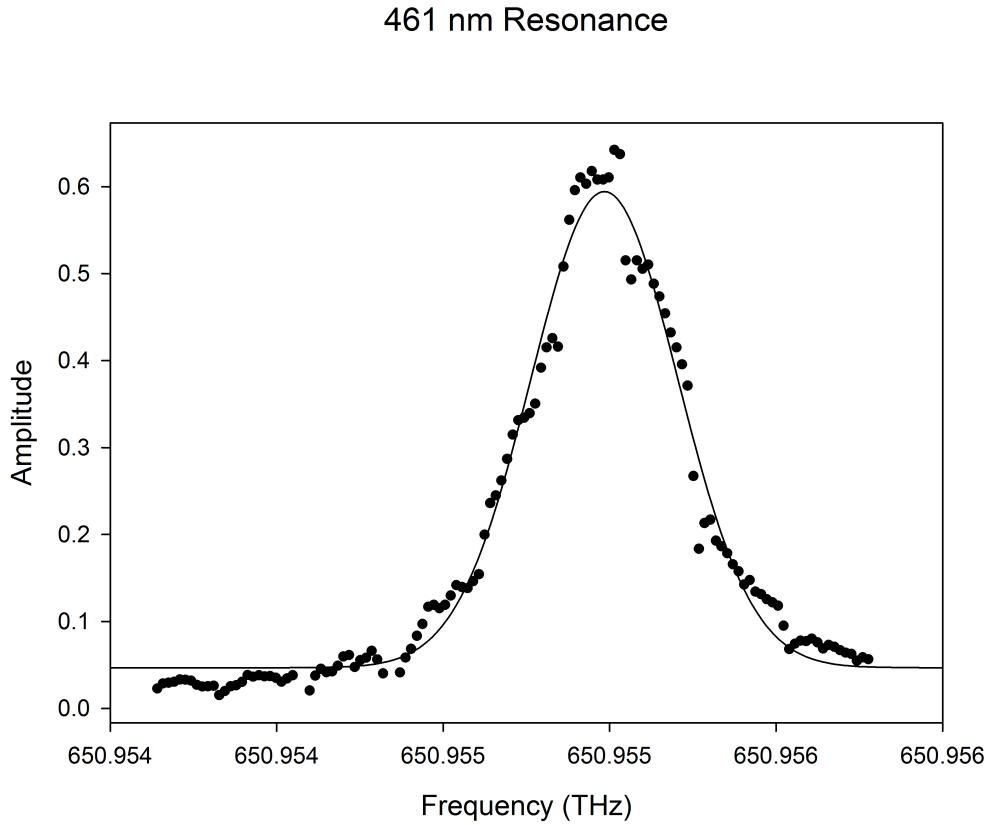

Figure 3.14: Scan of 461 nm radiation lineshape. Wavelength values converted to doubled frequency scan. A value of $\Delta\nu = 550$ MHz FWHM was determined for the resonance width.

calculated to be approximately $\Delta\nu = 550$ MHz. The width of the resonance is presumably dictated by the Doppler broadening of the atoms of the Sr oven source. This study concluded that the operation at the wavelength of $\lambda = (460.862 \pm 0.001)$ nm achieved optimal ionization and loading time.

3.5.2 Second Step Ionization Laser: 405 nm

The 405 nm diode used in the rf Paul trap loading process was a simple non-wavelength selected blue ray laser diode. Characterization of the diode was required to assess whether this particular diode met all the required characteristics for effective second step ionization of the strontium ion. The presence of autoionization resonances in the continuum spectrum of excitation from the 5p level allows orders of magnitude improvement in ionization efficiency if the 405 nm diode radiation falls within the resonance profile.

The desired characteristics of the diode to be in resonance with the strongest autoionization feature ($5p\ ^1P_1$ - $4d^2\ ^1D_2$) are:

$$f = 739.9332 \text{ THz}, \ \Delta\nu = 1.8 \text{ THz} \tag{3.1}$$

$$\lambda = 405.162 \text{ nm}, \ \Delta\nu = 0.985 \text{ nm} \tag{3.2}$$

Wavemeters were ineffective in accurately measuring the wavelength due to the broad emission of the 405 nm diode. A calibrated diffraction grating spectrometer was used to obtain a precise wavelength reading of 404.65 nm. A diode temperature and laser current study was then carried out on the diode to determine the optimal parameters for use.

This study concluded the diode becomes multi-mode at all laser currents higher than 41 mA. The 405 nm laser was chosen to be operated at 40 mA laser current emitting more than 15 mW of output power at the source. Figure 3.15 is a plot of amplitude as a function of frequency of the $5p\ ^1P_1$ - $4d^2\ ^1D_2$ resonance and the emission frequency of 405 nm laser when operated at the specified operating conditions. The output laser frequency lineshape, indicated with a dotted line, is barely visible at this resolution compared to the required ionization transition resonance shown. This result confirms that the laser excitation is sufficient within the resonance bandwidth for effective ionization, even when operated in multi mode regions at currents higher than 41 mA.

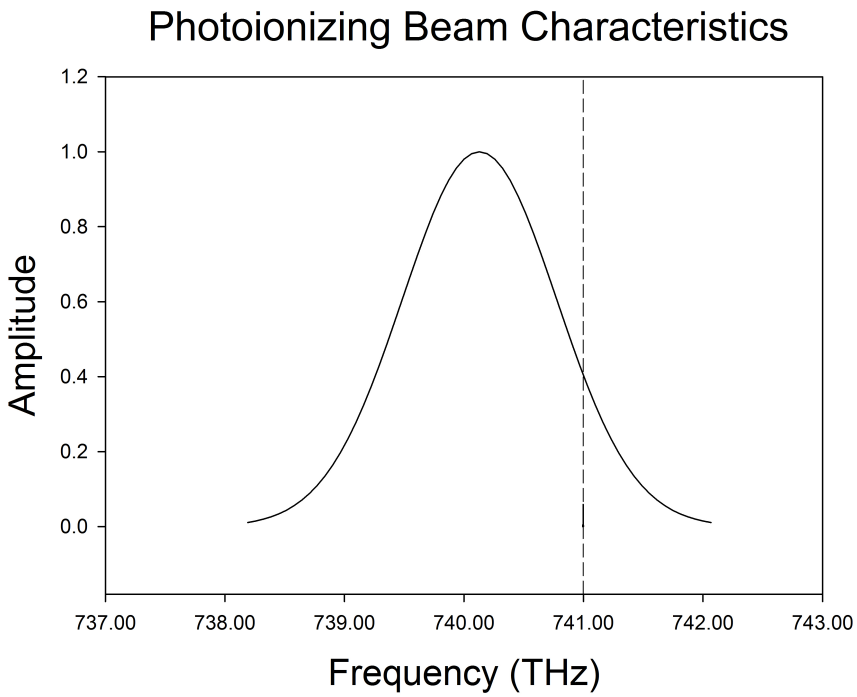

Figure 3.15: The relative ionization efficiency amplitude is shown as a function of detuning. The solid curve shows the variation of ionization efficiency due to the presence of the $5p\ ^1P_1$ - $4d^2\ ^1D_2$ resonance. The dashed curve shows the determined diode laser emission profile.

3.5.3 Improvement and optimization of beam focussing into the rf Paul Trap

The main radiations used in the current work are supplied to the rf Paul ion trap via fiber optic patch cords. They are combined together via a series of optical elements before being sent into the ion trap. Located in front of the trap vacuum enclosure entrance is a primary focussing lens system. The system consists of a negative achromat which expands the $w \approx 1$ mm radius beam followed by positive achromat lens designed to focus the radiation to a beam waist of 10's of μm at the trap center. It is critical that sufficiently small focal spots (giving high intensities) are achieved yet having a sufficient Rayleigh range of the focussed beam so that a minimum of scattered light is generated in the vicinity of the trap structure.

The original set up had a lens system located close to the trap magnetic shield entrance. Adjustment of the beam pointing was achieved by lateral displacement of the primary positive lens which was mounted on a flexure mount with micrometer adjustments. The

mechanical instability of the mount together with the rather small beam waists used resulted in the focal spot requiring readjustment approximately every hour. A new set up was designed to reduce alignment time and increase stability. The improvements of the new design involved: a) a new rigid mount consisting of four stabilizing steel rods holding the negative and positive lens mounts in fixed relative alignment with micron level tolerance, b) the implementation of new optics and a larger distance between the positive focusing lens and the trap entrance, and, c) the allowance for two pico-tilt translator mirrors immediately before shield entrance for easy beam alignment. The negative and positive lenses of the new system were chosen to achieve a tight waist of approximately $w_0 = 20$ μm. An in-house NRC Gaussian beam program, *Modes7*, was used to calculate the necessary parameters of the lenses.

Two different techniques were used to accurately determine the waist radius of the 422 nm beam propagating through the new optical setup, to ensure the setup is aligned such that the beam waist of approximately 20 μm was located at the ion. The knife-edge technique [41] was one of the methods used to calculate the waist of the 422 nm Gaussian beam radius w. This technique involves recording the power of the beam propagating along the z axis, as a knife-edge is translated across the beam along the x or y axis.

The normalized power transmitted after the edge can be expressed as:

$$P_N(x) = \frac{1}{2}\left[1 - \mathrm{erf}\left(\frac{\sqrt{2}(x - x_0)}{w_x}\right)\right] \tag{3.3}$$

where x is the position of the knife-edge with respect to x_0 the beam center position, and w_x is the beam radius calculated at position x. This equation is similar for measurements taken along the y axis as well. The measurements are taken at different distances, z, along the beam z axis, from a chosen origin of the positive focusing lens of the new setup. The different beam radii, $w(z)$ are calculated with the fitting equation 3.3, then the beam waist, w_0 can be found using the Gaussian beam equation:

$$w(z) = w_0\sqrt{1 + \frac{(z - z_o)^2}{z_R^2}} \tag{3.4}$$

where $w(z)$ is the beam radius at a given point on the z-axis, z is the distance of the knife-edge measurement from the origin, z_o is the beam waist position, and z_R is the Rayleigh range defined as:

$$z_R = \frac{\pi w_o^2}{\lambda} \tag{3.5}$$

Using these functions one can determine from the recorded data the beams waist, w_o and position, z_o [41].

Another method of calculating the beam waist was an aperture transmission technique. It involves measuring the power of a Gaussian beam transmitted through an aperture of known radius, r. Knowing the total power of the beam, P_T and the power that transmits through the aperture, $P(r,z)$, the beam radius, $w(z)$, can be determined. The beam radii can be found with the function [42]:

$$P(r,z) = P_T\left[1 - e^{-2r^2/w^2(z)}\right] \tag{3.6}$$

The beam radius for each measurement position can then be plotted using the fitting function 3.4, and the beam waist, w_0 can be found .

The knife-edge technique was used to determine the waist radius for the 422 nm radiation along the x and y axis as 22 ± 2 μm and 18 ± 1 μm respectively. This confirms the average beam waist as $w_0 = 20 \pm 1$ μm at the trap center, which is $z_o = 52.4 \pm 0.3$ cm from the positive lens. The 1092 nm repump beam was characterized in a similar manner using the aperture transmission technique. After several measurements using an aperture of radius $r = 50$ μm, the waist of the 1092 nm beam was calculated to be $w_0 = 54 \pm 1$ μm, at $z = 49.6 \pm 0.3$ cm from the positive focusing lens. The repump beam focuses slightly before the trap center, but it is still relatively focused at the trap center.

The improved ion trap beam focusing system is shown in Figure 3.16. The new setup has a f= -100 mm negative achromat held a distance of 23.5 cm from the primary f= +200 mm achromat focussing lens located about 52.5 cm from the trap center. Commercial [New Focus Pico motor] piezo tilt drives provide stable pointing to the two flat steering mirrors with little detectable sag or drift. With the improved optical system, operation of the experiment for muti-day periods could be achieved without adjustment of pointing.

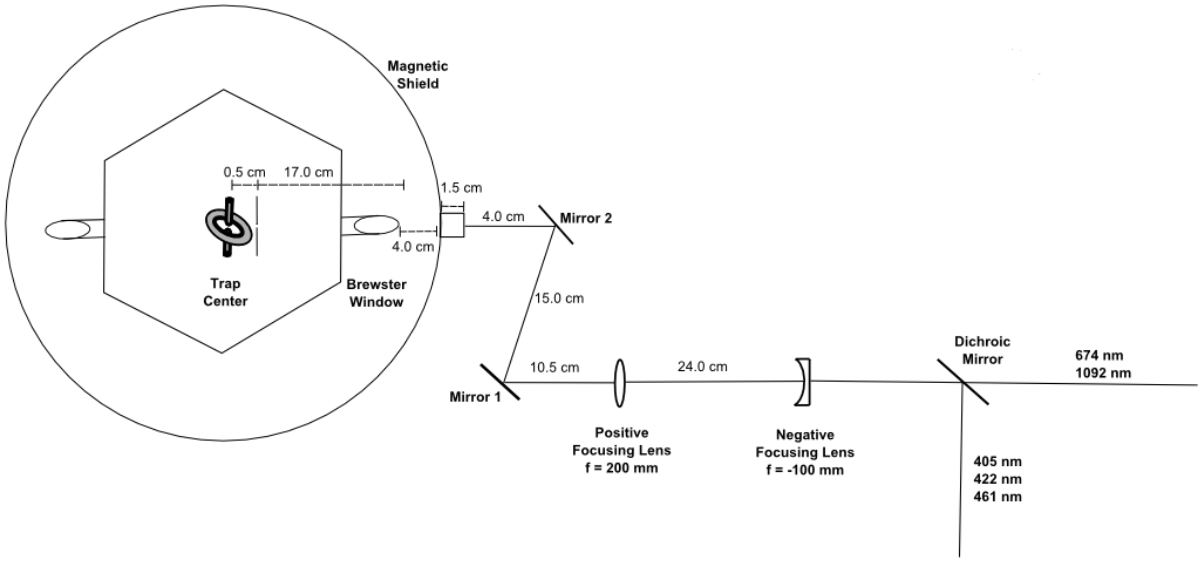

Figure 3.16: The rf Paul trap optical system setup

3.6 RF Paul Trap Fluorescence

As mentioned earlier, the 422 nm laser excitation is used not only for cooling the $^{88}Sr^{+}$ ion but for fluorescence detection of the clock transition using the electron shelving technique explained in Section 3.4. When an electron is 'shelved' in the $^{2}D_{5/2}$ level by excitation on the electric quadrupole allowed $5s\ ^{2}S_{1/2} - 4d\ ^{2}D_{5/2}$ clock transition, the $^{88}Sr^{+}$ is unable to absorb a 422 nm photon. The absence of fluorescence, a quantum jump, is used as an indication the ion has undergone excitation on the clock transition. Once excited into the upper state of the $S - D$ transition, the ion will typically decay by spontaneous emission to the ground state. The natural lifetime of the $4d\ ^{2}D_{5/2}$ state has been experimentally determined as $\tau = 390.8(1.6)$ ms in other work [32].

Figure 3.17 shows the quantum jumps observed in the fluorescence of the rf Paul trap when excited on the electric quadrupole transition. A clear contrast can be seen between the bright fluorescing state and the dark period providing unambiguous determination of the excitations. The distribution of dark periods correspond to the probability of decay of the metastable state and previous studies have shown that these follow an exponential distribution with the above stated lifetime [43]. In this work, improvements on the trap excitation and optical collection systems increased the detected photomultiplier fluorescence

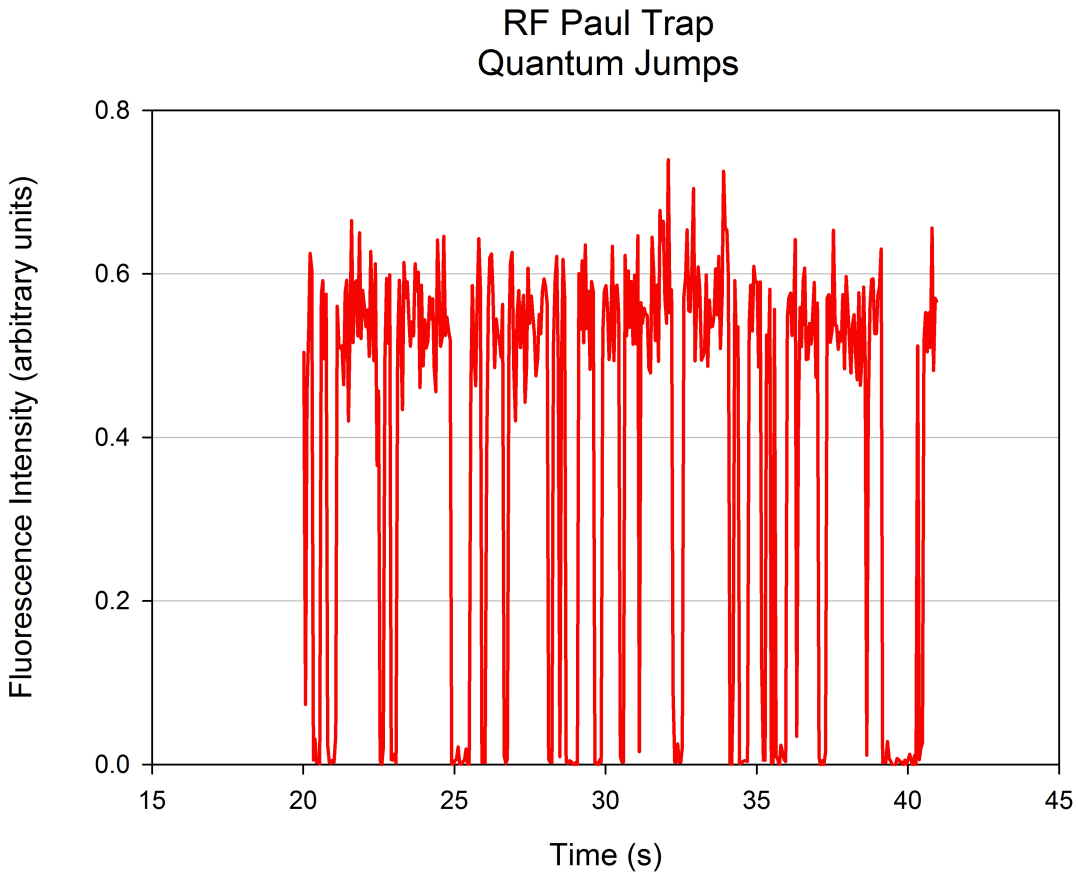

Figure 3.17: Quantum Jumps Observed in 422 nm Fluorescence

count rate from about 5 000 counts/s to 25 000 counts/s, and decreased the background scattering from about 500 counts/s to 50 counts/s. The increase in detected fluorescence rate arose from operating the trap with the improved excitation beam optics which allowed the ion to be excited at the optimum laser power intensities. In addition, the replacement of the 422-nm bandpass fluorescence filter of T=0.4 transmission with a specially designed bandpass filter of T=0.96 allowed greater efficiency of collected light from the available solid angle of observation. The reduction in the observed scattered background rate was primarily achieved via the improved beam focussing optics which had a larger focussed Rayleigh range over the trap dimensions together with the reduction of applied laser power which still yielded comparable fluorescence rates. With this setup, excitation of the reference $S - D$ transition can be achieved with low uncertainty of the fluorescing state level and shorter integration periods can be used for the detection phase to sense whether a transition has occurred.

4 Results

4.1 Classical Collisional Rates

In studies performed prior to the present work, sporadic quantum jumps were observed while the ion was fluorescing in the trap and unexposed to the clock transition excitation. These events of interrupted fluorescence are likely caused by the ion colliding with other gas molecules in the trap. These events not only cause false indications of transitions on the reference $S-D$ transition but set a limit on the duration an ion can remain in the trap. A collision may cause the loss of the ion from the trap due to such processes as charge transfer, weak binding, or ejection of the ion out of the trap potential. To identify the likelihood of these events happening, the classical collision rates of all the observed molecular species in the trap were calculated.

The gas molecules present in the vacuum chambers of both traps were found using their respective mass spectrometers which were mounted on each vacuum chamber. A spectrum of the partial pressures of each atomic mass unit from 1 to 44 was obtained, and the partial pressures for each significant gas species present were calculated. Using these partial pressures, the classical collisional rates of each gas molecule with the $^{88}Sr^{+}$ ion were calculated using the following method from Angular (momentum conserved) Average Dipole Orientation Theory (AADO) [44].

Using AADO theory, the collisional rate γ can be expressed with:

$$\gamma = \eta k_{AADO} \tag{4.1}$$

where k_{AADO} is the collisional constant, and the density, η. The density is found with the ideal gas law:

$$PV = nk_BT \Rightarrow \frac{n}{V} = \frac{P}{k_BT} = \eta \tag{4.2}$$

where the temperature is $T = 296$ K and the Boltzmann constant is $k_B = 1.38 \times 10^{-23}$ J/K. k_{AADO} is expressed as [44]:

$$k_{AADO} = \frac{2\pi q}{\mu^{1/2}} \left[\alpha^{1/2} + C\mu_D \left(\frac{2}{\pi k_B T} \right)^{1/2} + \frac{Z\mu_D I^{1/2}}{\alpha^{1/4}} \right] \tag{4.3}$$

where μ is the reduced mass of the gas with the $^{88}Sr^+$ atom, and the elementary charge is $q = 1.602 \times 10^{-19}$ C. The second and third parameters of equation 4.3 are negligible for most gases without a dipole moment, μ_D, except water and carbon monoxide. Also, $Z = 8.63 \times 10^{18}$ s cm$^{5/4}$ g^{-1}, C is the dipole locking constant, $C_{H_2O} = 0.26$ and $C_{CO} = 0.062$, and I is the moment of inertia of the dipole molecule rotation in a perpendicular plane to the dipole moment $I_{H_2O} = 1.0 \times 10^{-40}$ g cm^2 and $I_{CO} = 1.5 \times 10^{-39}$ g cm^2 [44]. The results for each ion trap are found in tables 4.1 and 4.2.

Table 4.1: The rf Paul trap: Partial pressures and collisional rates

Gas	Partial Pressure, (10^{-10} Pa)	Polarizability, α (10^{-24} cm^3)	Dipole Moment, μ_D	Collisional Rate Constant, k_{AADO} (10^{-16} m^3/s)	Collisional Rate, γ (10^{-4} s^{-1})
H_2	354.58	0.8		14.96	128.00
CH_4	9.53	2.6		10.25	2.36
H_2O	3.47	1.5	1.9	19.84	1.67
Ar	0.74	1.6		5.64	0.11
CO	381.80	2.0	0.11	7.42	68.41
N_2	7.43	1.7		6.62	1.19
CO_2	34.66	2.9		7.36	6.16
Total	792.21				207.90

Table 4.2: The endcap trap: Partial pressures and collisional rates

Gas	Partial Pressure, (10^{-10} Pa)	Polarizability, α (10^{-24} cm^3)	Dipole Moment, μ_D	Collisional Rate Constant, k_{AADO} (10^{-16} m^3/s)	Collisional Rate, γ (10^{-4} s^{-1})
H_2	102.44	0.8		14.96	37.01
He	17.17	0.2		5.35	2.23
CH_4	4.96	2.6		10.25	1.23
H_2O	2.83	1.5	1.9	19.84	1.35
Ar	0.63	1.6		5.64	0.09
CO	51.59	2.0	0.11	7.42	9.24
N_2	0.00	1.7		6.61	0.00
CO_2	7.90	2.9		7.36	1.40
Total	187.52				52.55

Hydrogen is one of the dominant gas species present in the background gas environment for the ion. The hydrogen arises primarily from the emission of the gas trapped within the metal surfaces of the chamber. Special treatment by high temperature bakeout was applied to the endcap trap system and one can see the significant reduction of the gas in the endcap trap vacuum environment.

These results concluded that the total classical collisional rate of the rf Paul trap to be $\gamma = 208 \times 10^{-4}$ s^{-1} giving a combined rate of a collision occurring every 48 s, and in the endcap trap the total classical collisional rate was $\gamma = 52.6 \times 10^{-4}$ s^{-1} with a combined rate of a collision occurring every 190 s. The uncertainty on these values are considered to be about 20%, mainly due to the uncertainty of measuring the partial pressures in the trap. The higher collision rates observed in the rf Paul trap are consistent with the mean lifetimes of the ion in the rf Paul trap compared to the endcap trap. The ion residence lifetime in the endcap trap can span several day periods whereas the rf Paul trap can rarely contain an ion longer than 24 hr in duration. Using the previously determined shift per unit pressure as 8×10^4 Hz/Pa [3], calculations for the frequency shift of the clock transition

due to the collisions indicate that the shifts should be below the 1 mHz level (2×10^{-18}) for the endcap trap and the 4 mHz level (8×10^{-18}) level for the rf trap system.

4.2 Observed Micromotion

As described earlier, micromotion is the driven movement of the ion due to the applied ac electric field in the trap can be the largest contributor of frequency shifts and uncertainty if not effectively minimized. In theory, micromotion should disappear when the ion is in the center of the trap where there is no electric field, but as explained in Section 2.4, several effects cause micromotion. The applied potentials to the electrodes in both traps are adjusted to the optimal voltage where micromotion is minimized. The techniques used to perform the micromotion studies are different for the rf Paul trap and the endcap trap. This is primarily due to the limitations for one dimensional probing of the micromotion for the rf Paul trap and the availability of three mutually orthogonal observation directions in the endcap trap system.

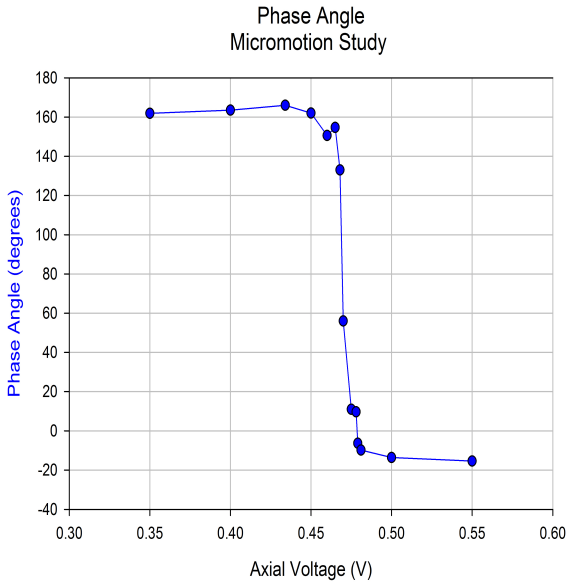

Figure 4.1: Micromotion study of the detected photon correlation with phase angle of the trap drive as a function of axial DC bias in rf Paul trap. The phase flip is at 0.48 V.

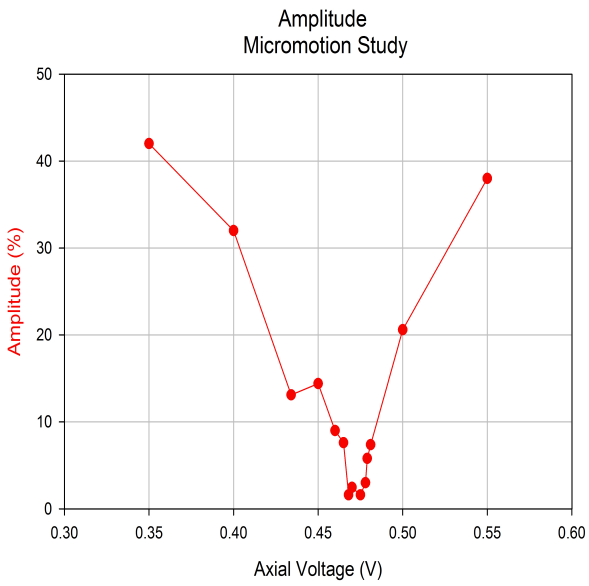

Figure 4.2: Micromotion study of the detected photon correlation amplitude in rf Paul trap as a function of the axial DC bias. The lowest amplitude is 1.1% at 0.47 V.

A study reducing the micromotion in the rf Paul trap, set to the 'magic' trap frequency of $\Omega_0/2\pi = 14.39(25)$ MHz, is shown in Figures 4.1 and 4.2 using data from a previously developed program. Here the correlation between the fluorescence photon arrival time relative to the trap voltage drive phase is measured. Both Phase and Amplitude of the correlation are calculated. When strong micromotion occurs, the ion will be driven back and forth in space with the applied field and suffer Doppler shifts relative to the incoming excitation beam. The Doppler shifts will then modulate the fluorescence scatter rate which is observed as a correlation of the arrival time of the photons with the trap driving field phase. The setup for this trap has DC voltage adjustments for the ring electrode potential (symmetry voltage) and the axial potential difference.

For this study, the symmetry voltage was set to zero, and the axial potential was varied, obtaining optimization of micromotion. This occurs at the phase angle flip, where the ion crosses the equatorial plane of symmetry of the trapping field (see Figure 2.1), and the point of lowest amplitude of the oscillation of the ion along the 422 nm beam direction.

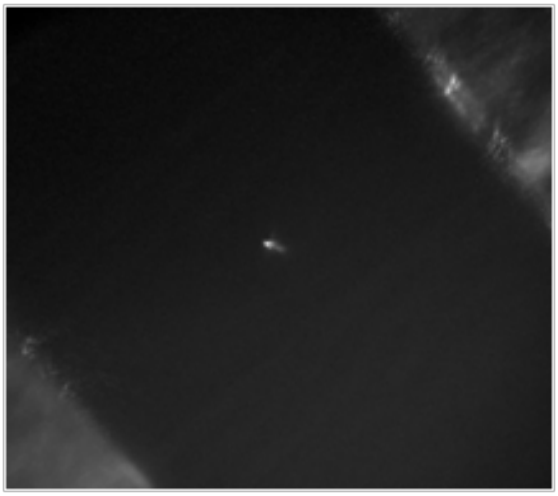

Figure 4.3: The $^{88}Sr^{+}$ ion fluorescence seen with camera in endcap trap (photo courtesy of P. Dubé).

As described, the endcap trap system has an image intensified CCD camera which allows observation of the central trap region at high magnification. A coarse adjustment minimizing the micromotion can be performed by monitoring the ion motion visually, see Figure 4.3. The DC trim electrode voltages were varied until the micromotion was reduced in the image plane of the camera, however the motion along the viewing axis of the camera cannot be directly seen.

Final quantitative measurements of the micromotion amplitude along a particular excitation beam direction can be obtained by examining the intensity of the frequency sidebands imposed on a transition at the trap drive frequency [3]. This is due to the driven motion at the trap drive frequency causing a periodic Doppler shift of ion and thus modulating the spectrum to create a carrier and sidebands. Probing at the 674 nm reference transition is

used since the width of the transition is much narrower than the MHz level micromotion frequency sidebands and thus such sideband to carrier intensity ratios can easily be resolved and measured.

This type of study was performed on the endcap trap system allowing full three dimensional reduction of direct micromotion shifts of the ion. The final micromotion induced shifts on the $S - D$ transition frequency were then determined to be at the few parts in 10^{-18} level [3]. However, the measurements on the rf Paul trap are limited to only one probe direction and cannot sense the complete micromotion level. As shown in Figure 4.4 small motional sidebands are observed relative to a particular Zeeman component located at positive and negative detuning of the trap drive frequency. By measuring the relative sideband to carrier height and using the relations developed in [3], one can determine the observed root mean squared electric field the ion is exposed to along the compensated probe beam direction. Where, for a small modulation index β_i, the integrated carrier to sideband ratio is:

$$R_i \cong \frac{\beta_i^2}{4} \tag{4.4}$$

$$\beta_i = \left(\frac{\omega_0}{\Omega}\right) \frac{|\hat{n}_i \cdot v_0|}{c} \tag{4.5}$$

where ω_0 is the probe laser angular frequency, Ω is the trap frequency, c is the speed of light, $\hat{n}_i$ is a unit vector along the beam propagation direction, and v_0 is the vector amplitude of the ion velocity. From this the electric field can be determined as:

$$E_0 = \left(\frac{m\Omega}{e}\right) v_0 \tag{4.6}$$

The mean squared value of the electric field summed over all three orthogonal directions is expressed as [3]:

$$\langle E^2(t) \rangle = 2 \left(\frac{m\Omega^2 c}{e\omega_0}\right)^2 \sum_{x,y,z} R_i \tag{4.7}$$

Results for the only direction of observation give a value of $\mathrm{E}_{beam,rms} = 0.15$ V/cm. However, since micromotion shifts arise from the total value of E_{rms} summed over all three

orthogonal directions, the actual value can be considered to be much larger for the rf trap due to significant contributions along the non compensated directions.

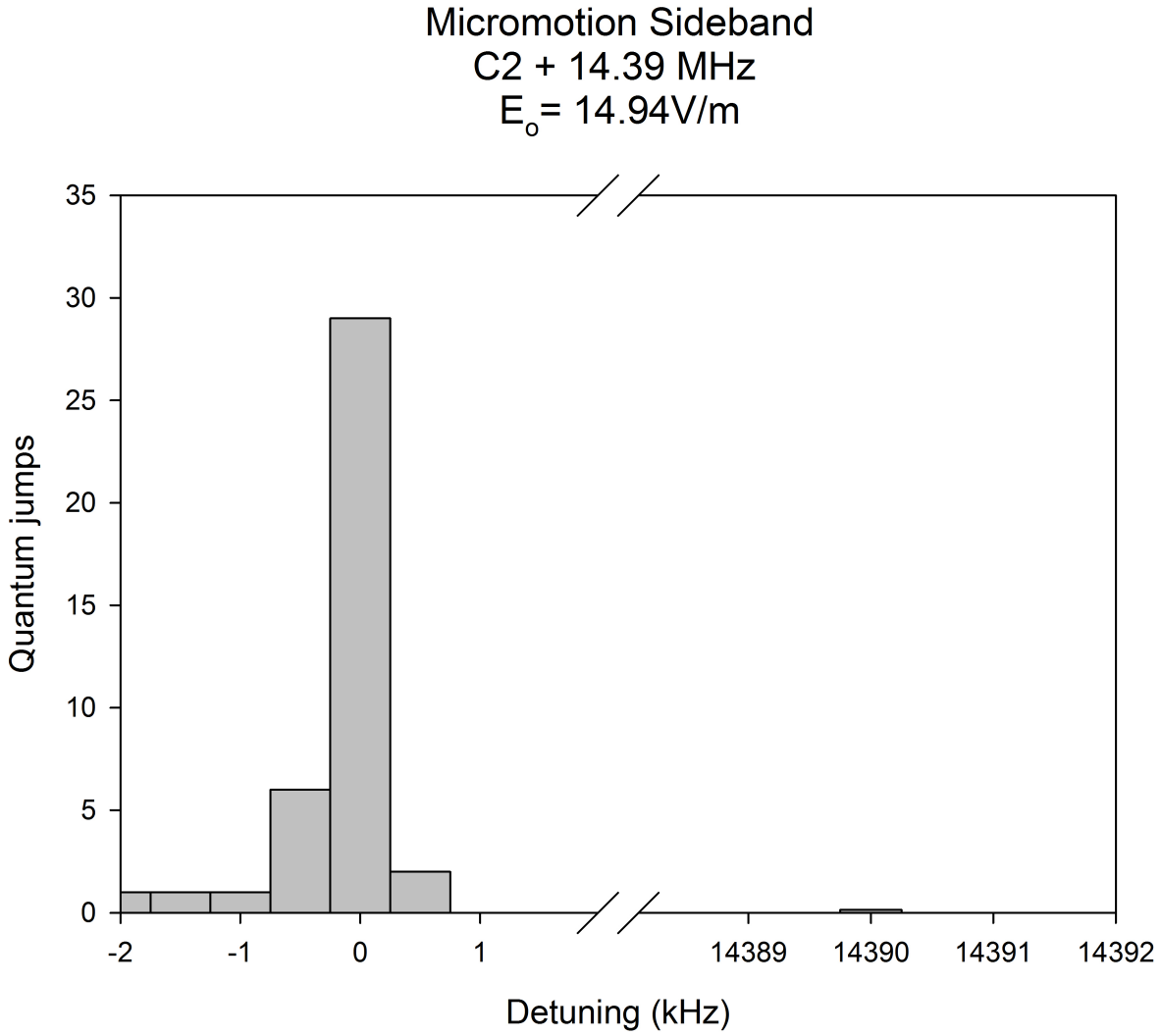

Figure 4.4: A $^{88}Sr^{+}$ S-D transition Zeeman component and upper micromotion sideband at the detuning of the trap drive frequency of 14.39 MHz.

For both traps, the positions for minimum micromotion varied slightly with every experiment, therefore micromotion was minimized before every comparison of the ion center frequency.

4.3 Ion Temperature in the rf Paul Trap

The $^{88}Sr^{+}$ ion possesses thermal kinetic energy, despite Doppler laser cooling and micro-motion minimization, while being confined in the three dimensional harmonic potential of the rf Paul trap. The thermal energy results in a secular motion of the ion inside the trap potential. The secular frequencies are given by the depth of the potential well along the three principal axes of the trap.

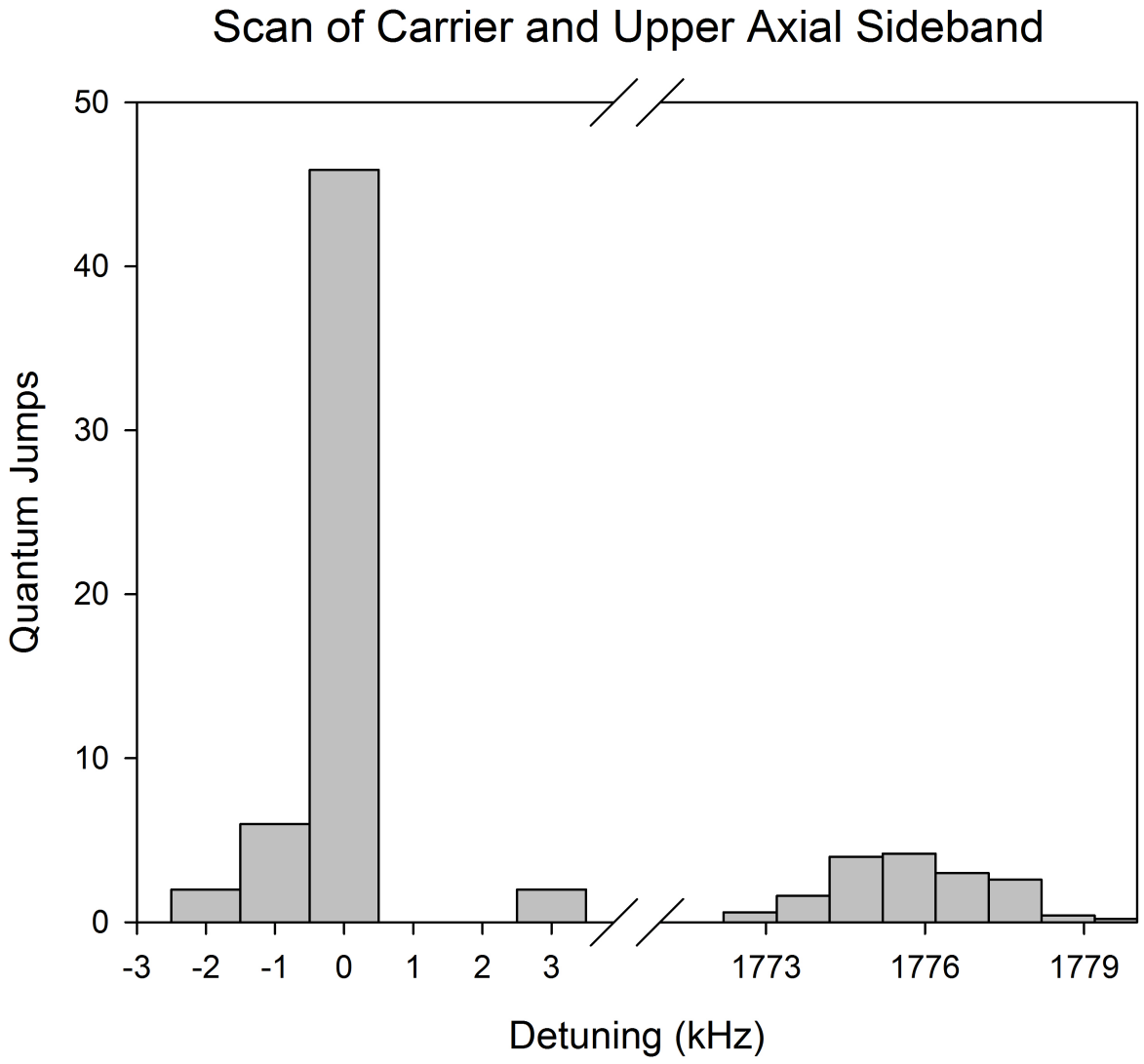

Figure 4.5: Frequency scan of a Zeeman component and upper secular sideband. This carrier to sideband ratio resulted in an estimated axial ion temperature of 7 mK.

The carrier frequency is the line center of a particular Zeeman component observed with the probe laser at 674 nm. The components of the periodic secular motion along the laser propagation direction, $\hat{\mathrm{k}}$, will result in carrier frequency sidebands at integer multiples of the secular frequencies. There are also sidebands corresponding to the linear combinations of the secular frequencies that must be accounted for in the analysis of the spectrum. If the sidebands are located at a greater distance from the carrier than its linewidth, the sidebands can be observed in the ion's spectrum, seen in Figure 4.5. Since the first order sideband is the strongest, it is the one used to monitor the ion motion and its temperature in this evaluation. As the velocity and temperature of the ion are reduced, the carrier amplitude increases while the first order sidebands amplitudes decrease. The carrier to sideband intensity ratio is related to the secular motion amplitude, which is related to the ion's temperature. With the measurement of this ratio, the ion temperature can be obtained [26].

In the usual case of $k_BT >> h\nu_i$, where T is the effective ion temperature and ν_i is the secular motion frequency of the ion, the relative intensity of the mth-order sideband to the carrier is given by [26]:

$$\left[\frac{\sigma(m)}{\sigma(0)}\right]_i = \left(1 + \frac{h\nu_i}{2k_bT}\right) \frac{I_m[(\frac{k_i^2 h}{4\pi^2 M\nu_i})(\frac{k_BT}{h\nu_i} - \frac{1}{2})]}{I_0[(\frac{k_i^2 h}{4\pi^2 M\nu_i})(\frac{k_BT}{h\nu_i} - \frac{1}{2})]} \tag{4.8}$$

where I_m is the modified Bessel function of order m, h is Planck's constant, k_B is Boltzmann's constant, T is the effective temperature, M is the ion mass, k_i is the component of the wave vector in the i direction, and $i = x, y, z$ are the trap's mutually orthogonal axes. In the present setup, the wave vector components are calculated using the angles between k and the trap axes of the axial (z) and one radial (x) direction in the rf Paul trap with $k = \frac{2\pi}{\lambda}$, are given:

$$k_z = k\cos(41.7^\circ)\cos(31.15^\circ) = 5.96(6) \times 10^6\ m^{-1} \tag{4.9}$$

$$k_x \approx k\sin(41.7^\circ)\cos(31.15^\circ) = 5.31(6) \times 10^6\ m^{-1} \tag{4.10}$$

Making the approximation $1 + \frac{h\nu_i}{2k_BT} \approx 1$ in equation 4.8, the temperature can be obtained:

$$T \approx \frac{4u\pi^2 M\nu_i^2}{k_i^2 k_B} \tag{4.11}$$

where u is calculated from the expression:

$$\frac{\sigma(m)}{\sigma(0)} \approx \frac{I_m(u)}{I_0(u)} \tag{4.12}$$

A series of studies were done to observe which parameters optimized the ion's kinetic temperature. The varied parameters were the frequency detuning of the 422 nm laser cooling radiation, the intensity of the 422 nm radiation, the intensity of the 674 nm probe radiation, and the applied symmetric voltage on the trap. In these studies, the beam intensities were adjusted by attenuating the beam with neutral density (ND) filters. The results can be seen in Figures 4.6, 4.7, and 4.8. All studies presented show the measured ion axial kinetic temperature and it is assumed the radial temperature is equivalent.

The first study, seen in Figure 4.6, demonstrates the effect of varying the 422 nm frequency detuning resulting in ion kinetic temperature changes. For this study, the powers of the 422 nm and the 1092 nm beams were kept at constant attenuation. Detuning the 422 nm frequency provided a seemingly significant effect, but with a large uncertainty, on the ion temperature. The lowest temperature of 14 $\pm$ 5 mK occurred at a frequency detuning of -12 MHz. This is quite close to the halfwidth at half maximum detuning for the $S - P$ transition where simple Doppler broadened laser cooling theory would predict the optimum cooling rate.

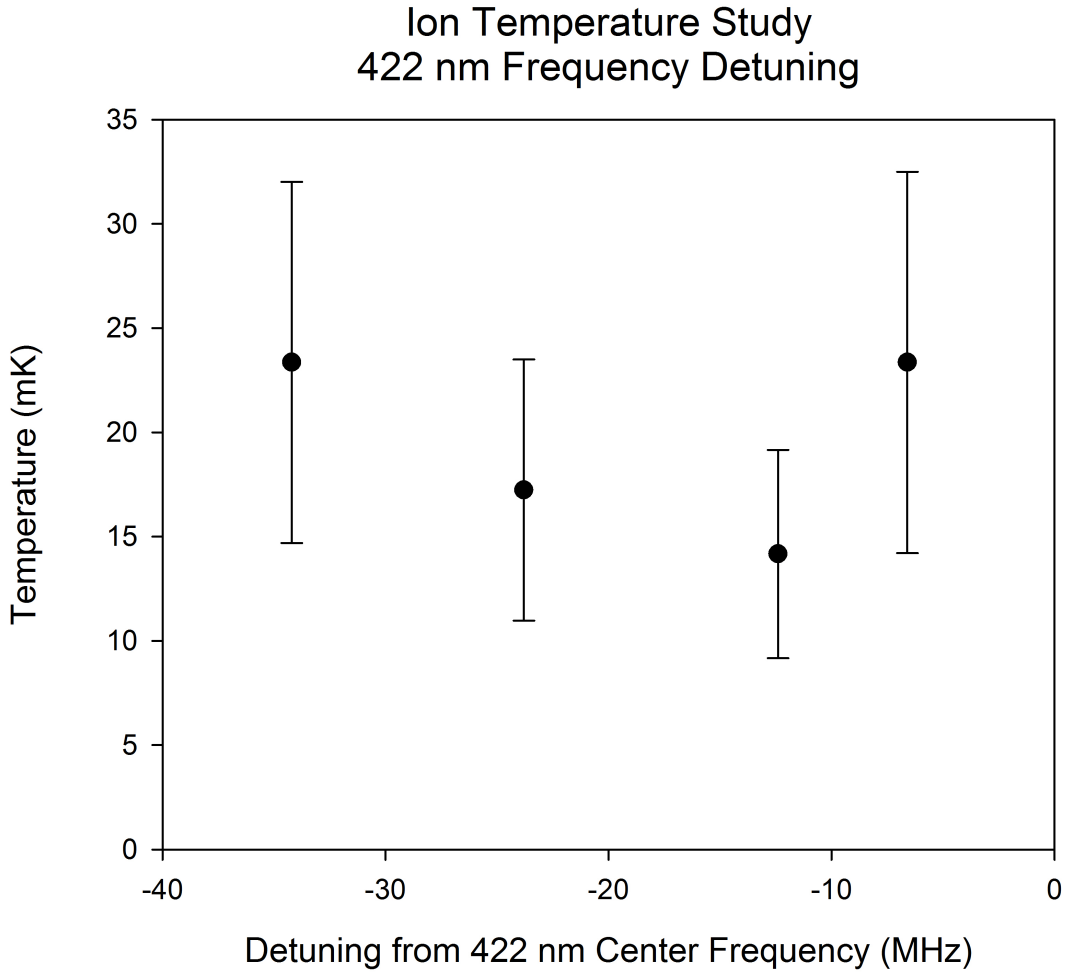

Figure 4.6: Plot of ion temperature as a function of 422 nm frequency detuning from the $S - P$ linecenter. All other beams were kept at a constant attenuation

The second study, Figure 4.7 is a study of intensity variation of the 422 nm cooling beam on ion axial temperature. Here the intensity is given in units of the strength of excitation (Rabi frequency) for the transition normalized by the excited P state decay rate [45]. While the $^{88}Sr^{+}$ is being cooled and repumped by the 422 nm and 1092 nm, it continuously undergoes the process of stimulated emission and re-absorption. In sufficiently coherent systems, this process can create oscillations in the ground to excited state population difference known as Rabi oscillations and characterized by a Rabi frequency, Ω.

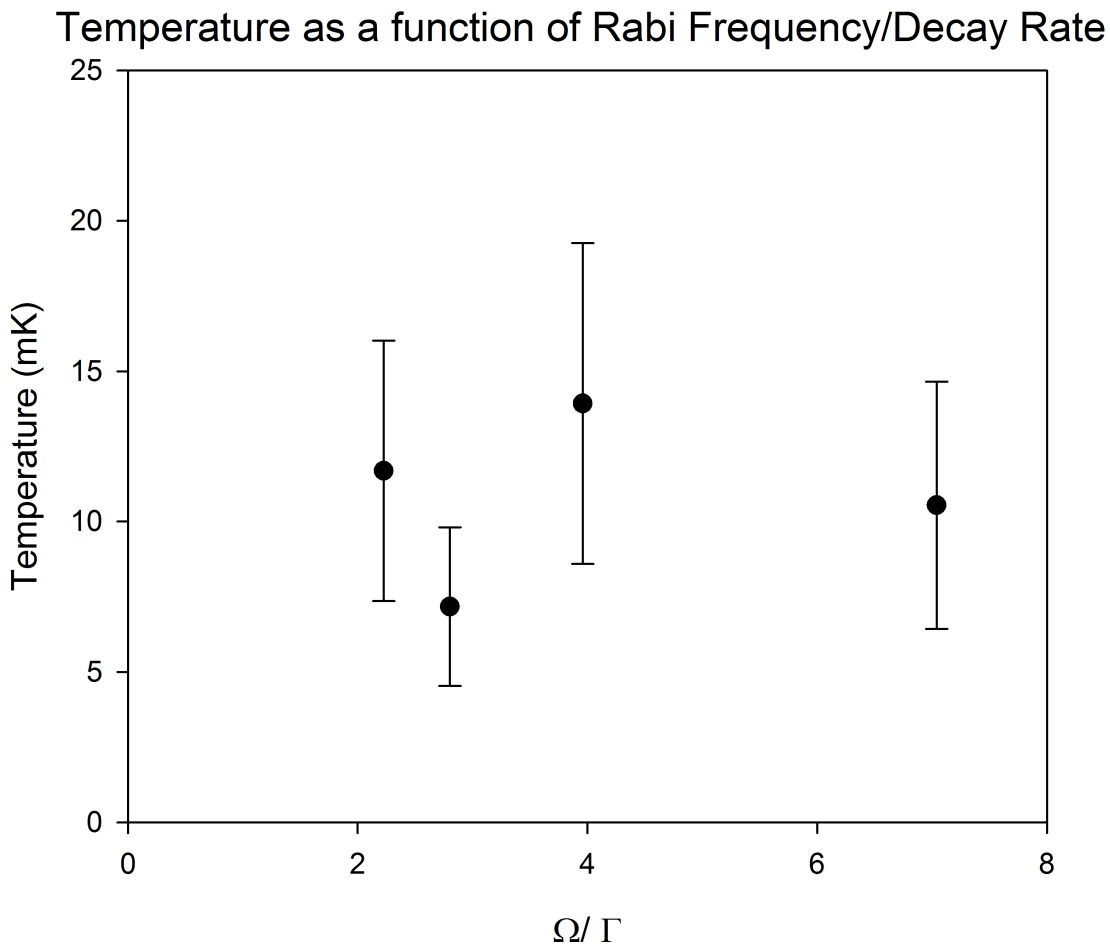

Figure 4.7: Plot of ion temperature as a function of Ω/Γ for the 422 nm $S-P$ transition. The 422 nm intensity was varied and represented has a function of Rabi frequency normalized by the excited state population decay rate.

The Rabi frequency is proportional to the electric field, E, of the incident beam and is defined by:

$$\Omega = \frac{\mu E}{\hbar} \tag{4.13}$$

where μ is the transition dipole moment, determined experimentally as 2.6096×10^{29} C m [45], and $\hbar$ is the reduced Planck's constant. The electric field is related to the known intensity of the 422 nm beam by:

$$I = \frac{c\epsilon_0}{2n}|E|^2 \tag{4.14}$$

where I is the intensity of the light, c is the speed of light, ϵ_0 is the permittivity of free space, and $n = 1$ is the value of the refractive index of vacuum. The intensity of a Gaussian laser beam is related to its power by the equation:

$$P_0 = \frac{I_0 \pi w^2}{2} \tag{4.15}$$

where w is the Gaussian beam radius at its waist given in section 3.5.3 as $w_0 = 20$ μm. Using equations 4.14, 4.13 and 4.15, where A is the optical density of the ND filter applied, the Rabi frequency can be shown as:

$$\Omega = \frac{\mu E}{\hbar} = \frac{\mu}{\hbar}\sqrt{\frac{2I}{c\epsilon_0}} = \frac{2\mu}{\hbar w}\sqrt{\frac{P_0 10^{-A}}{c\pi\epsilon_0}} \tag{4.16}$$

Equation 4.16 represents the Rabi frequency as a function of the filter attenuation applied to the beam. Figure 4.7 shows the intensity of the 422 nm as a function of Rabi frequency normalized by the decay rate of $\Gamma = 135.58\times10^6$ s^{-1}[45]. This ratio is important for studying the dark state formation in the $^{88}Sr^+$ ion caused by the cooling and repumping lasers, as explained in Section 4.4. Previous studies recommend a value of $\Omega/\Gamma \approx 1$ [45], however this study concluded that the dependence was quite insensitive for the range of powers used. The lowest temperature of 7 mK was obtained at $\Omega/\Gamma = 3\pm1$.

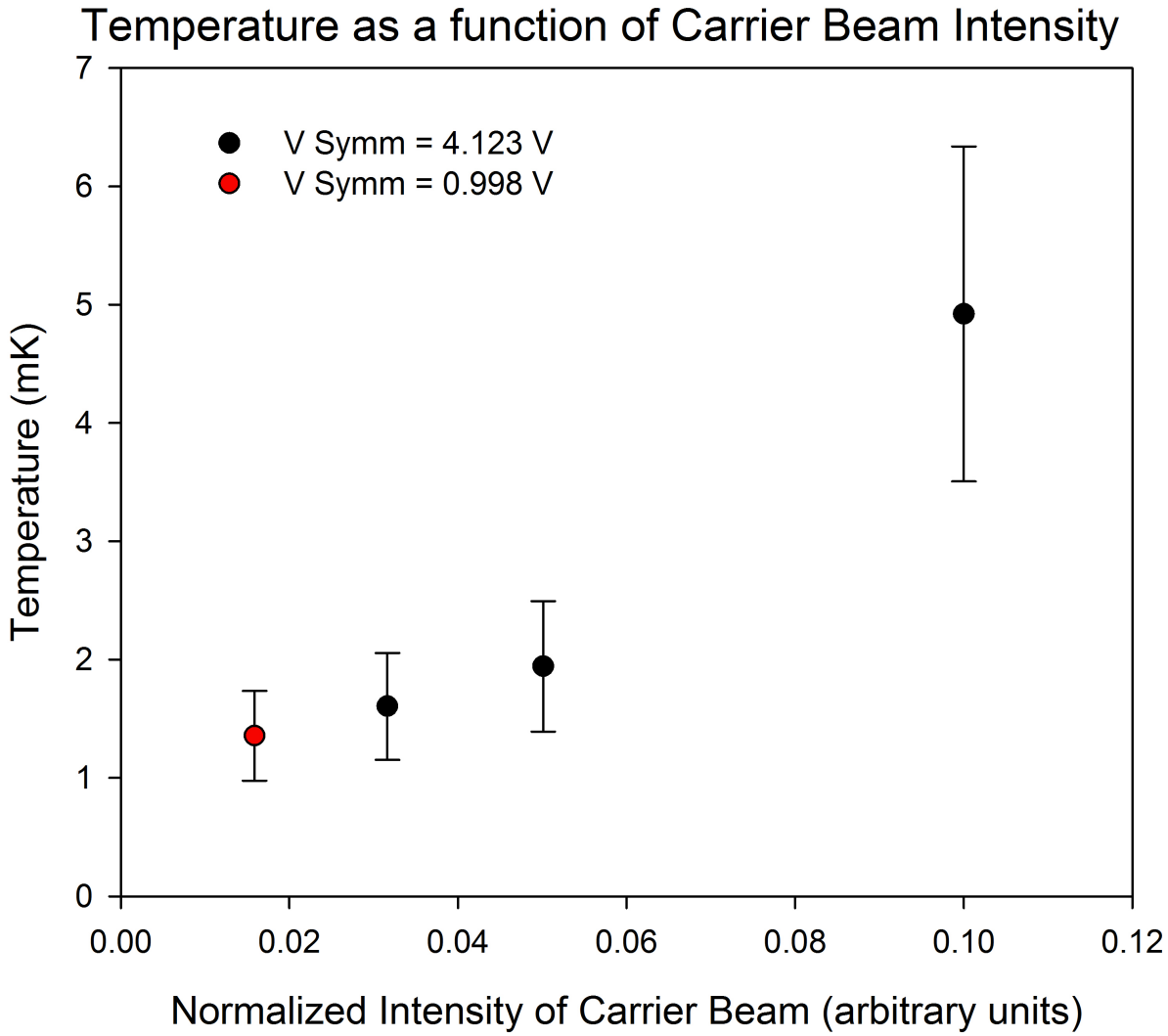

Figure 4.8: Plot of ion temperature as a function of 674 nm probe beam intensity. A symmetry potential was also applied to the trap.

It was found that the application of a non-zero symmetry voltage provided a further dramatic reduction in the ion kinetic temperature relative to the previously shown studies which were performed at $V_{sym} = 0$. The origin of this effect is not completely understood but may be due to improved laser cooling via removal of degeneracies of the harmonics of the radial oscillation frequency with those of the axial frequency. Theoretical studies have indicated that such degeneracies could limit ion temperature in laser cooling [46].

The third study seen in Figure 4.8 shows the study of the 674 nm beam intensity on the determined ion temperature with the non-zero values of symmetry voltage applied. The

422 nm and 1092 nm radiations were kept at a constant attenuation. The 422 nm frequency detuning was -11.9 MHz. The black points were all taken with an applied symmetry voltage of 4.123 V. The red point, with the lowest recorded temperature of 1.35 ± 0.38 mK, was taken with an applied symmetry voltage of 0.998 V. This low temperature point appears to be a result of the continuing trend of the decreasing ion kinetic temperature values with reduced probe beam intensity. The origin of this effect is considered to be the saturation of the carrier line height when too much 674 nm excitation is applied to the ion. It is thus important to perform such studies with the lowest possible probe intensities so as not to distort the actual carrier to sideband ratio.

Overall the lowest optimized ion temperature obtained was 1.35 ± 0.38 mK. The uncertainties considered were those of the wave vector projection and the variable u characterizing the carrier to sideband ratio. The uncertainty of the wave vector was due to inaccuracies in the known rf Paul trap angles for the incident beam. The uncertainty of the variable u was calculated by propagating the uncertainties of the observed sideband to carrier transition rates and the uncertainty in the quantum jump counts. The filters were not calibrated and therefore had an approximate percent error of 20%.

The main contribution to the shift of the ion reference transition due to ion thermal motion is via the time dilation (also known as second order Doppler shift) due to the ion's movement. It has been shown [3] that the fractional second order Doppler shift of the clock transition can be given as:

$$\frac{\Delta_{D2,s}}{\nu_o} = -\frac{3k_B T}{2mc^2} \tag{4.17}$$

where T is the secular motion temperature, k_B is Boltzmann's constant, m is the mass of the ion, and c being the speed of light.

For the given ion kinetic temperature of 1.4 ± 0.4 mK, the ion's reference transition would thus be expected to be shifted by: $\frac{\Delta_{D2,s}}{\nu_o} = 2(1) \times 10^{-18}$. This series of studies successfully allowed operation of the ion reference under conditions where the thermal contribution of the ion's kinetic temperature provided optimal reduction of the second order Doppler frequency shift.

4.4 Single Ion Lineshape Power Broadening and Dark State Formation

As previously mentioned, the $^2S_{1/2}$ - $^2P_{1/2}$ transition is used for Doppler cooling and detection with 422 nm radiation, and the $^2D_{3/2}$ - $^2P_{1/2}$ transition is excited with the 1092 nm beam to repump the ion out of the metastable $^2D_{3/2}$ state. Separately, both of these transitions were considered as two-level systems. However because they share the common $^2P_{1/2}$ state, it is actually a three-level system with the potential for quantum interference effects occurring. An example of quantum interference is coherent population trapping (CPT) which occurs when a three-level system is excited by two lasers simultaneously, coupling two states and forming a dark superposition state. When the ion is formed in such a dark state it is transparent to both lasers, because it can no longer emit or absorb photons.

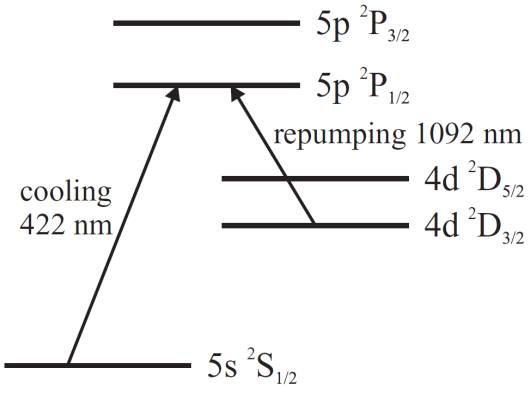

Figure 4.9: Three level system in the $^{88}Sr^+$ ion.

In this experiment, the $^2S_{1/2}$-$^2P_{1/2}$-$^2D_{3/2}$ system in the $^{88}Sr^+$ ion, shown in figure 4.9 [45], dark states are formed by the superposition of the Zeeman sublevels of the ground $^2S_{1/2}$ state and the metastable $^2D_{3/2}$ states and are unable to be coupled to the $^2P_{1/2}$ state via laser interaction. The fluorescence of the $^{88}Sr^+$ is disturbed by the formation of this dark state. Given that these states are detrimental to efficient ion cooling and detection, some studies of the ion lineshape were performed to examine the phenomena.

The CPT resonances of the coupled ground and metastable states can be distinguished experimentally by sweeping the detuning of either the 422 nm or the 1092 nm beam, shown in figures 4.10 and 4.11. The coherence dips seen in the fluorescence of these figures is a result of CPT. The location of the CPT resonance occurs where the detuning of both lasers from the intermediate P state are equal:

$$\Delta_{SP} = \Delta_{PD} \tag{4.18}$$

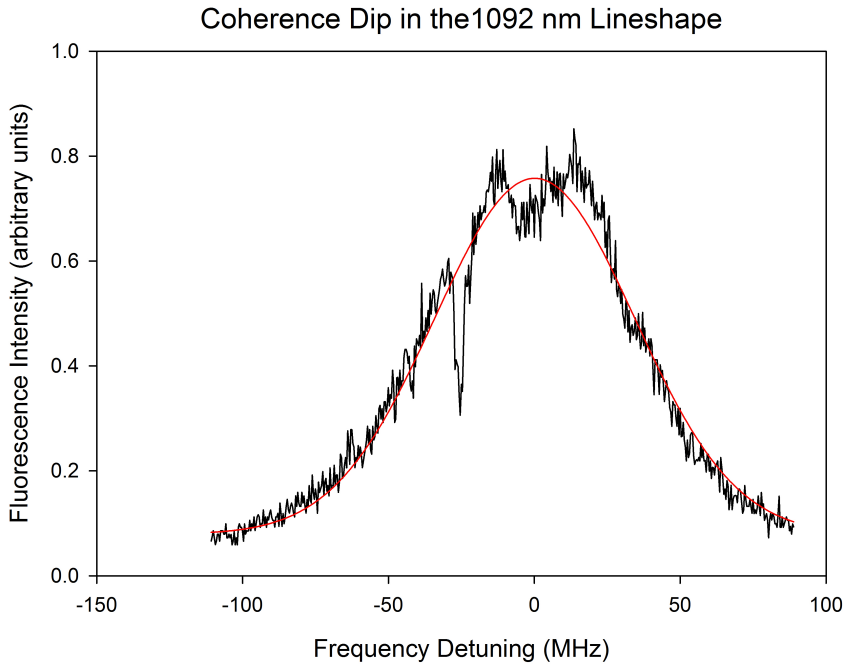

Figure 4.10: Sweep of 1092 nm beam detuning showing the $D_{3/2}-P_{1/2}$ lineshape with a coherence dip caused by interaction with the 422 nm radiation. The superimposed red line is the Lorentzian lineshape of the beam, ignoring the coherence dip.

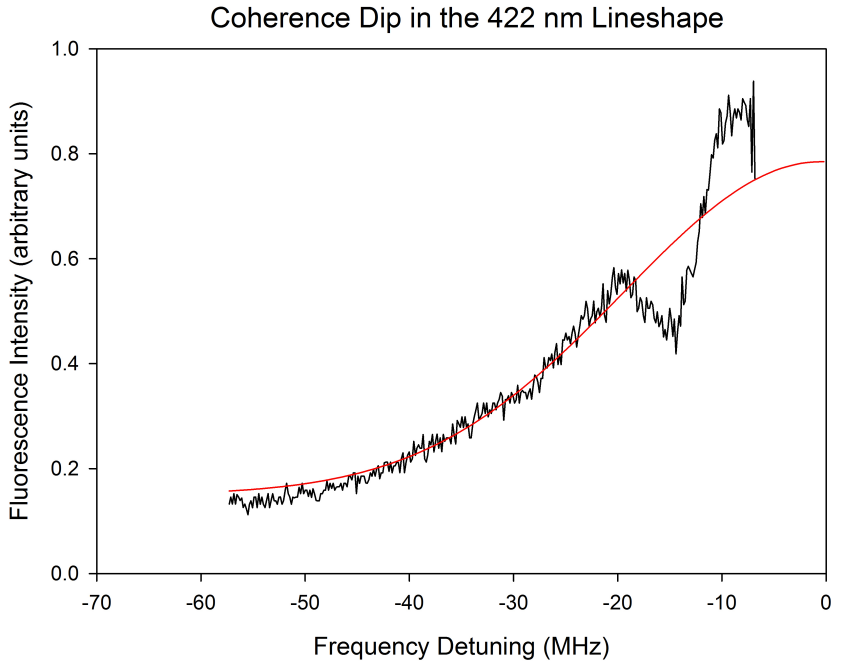

Figure 4.11: Sweep of 422 nm beam detuning showing the lower half of the $S_{1/2}-P_{1/2}$ lineshape with quantum interference features caused by interaction with the 1092 nm beam.

In practice, the repumper frequency should be placed at a positive detuning as the cooling beam is already red detuned for Doppler cooling. Also, the laser intensities are adjusted to obtain Rabi frequencies that result in acceptable scattering rates with minimal power broadening, as the laser linewidths are correlated to the CPT resonances [45].

It is apparent that the power broadening caused by the cooling and repump beam's linewidths is an important factor when considering the $^{88}Sr^{+}$ ion's dark state formation and temperature. A study on the power broadening of the 1092 nm transition was performed by varying the attenuation to investigate the point of saturation and the point of sharpest FWHM linewidth. From Figure 4.12 it was determined that at the lowest 1092 nm beam intensities a resonance of 57 MHz wide was obtained.

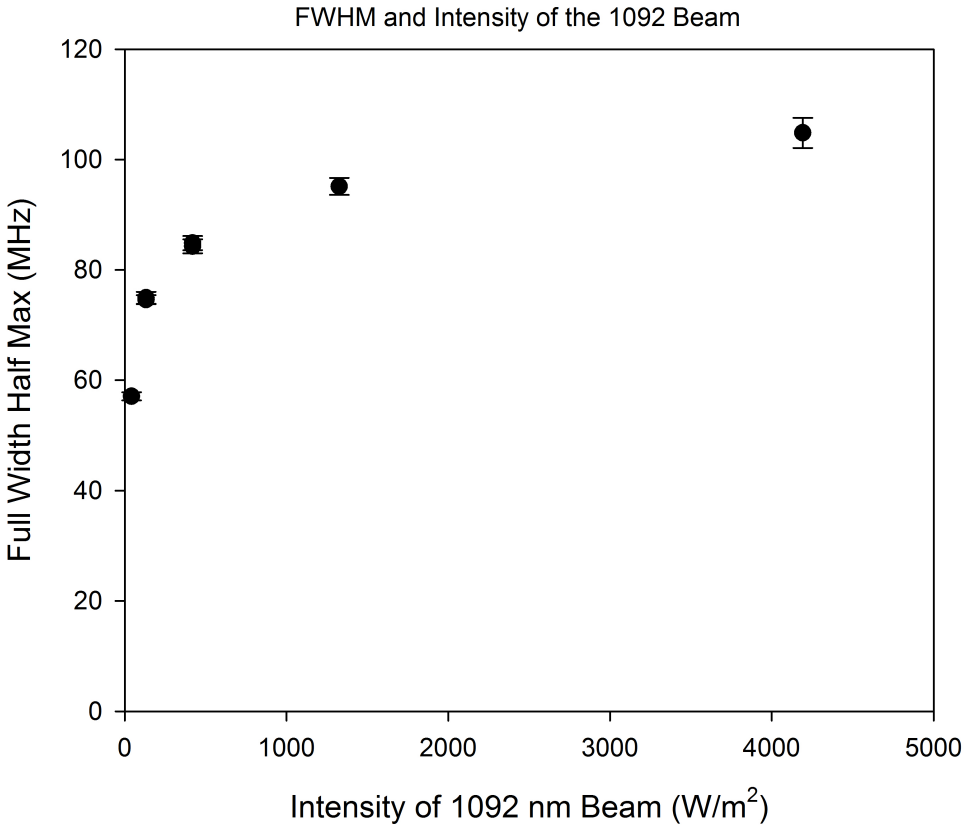

Figure 4.12: The FWHM of the $P - D$ resonance as a function of intensity of the 1092 nm beam. The 422 nm beam was held at a constant attenuation.

As mentioned in section 4.3, a previous study in [45] recommended operating the experiment with Rabi frequencies such that the value of $\Omega/\Gamma \approx 1$. This theoretically calculated value is said to optimize the scattering rate, while only broadening the linewidth by approximately 15%. The study in Figure 4.7 tests the ideal value for this specific experiment in the rf Paul trap. For future reference it should be noted that the beams powers can be adjusted to achieve the desired $\Omega_{c,r}/\Gamma$ ratio, where Ω_c and Ω_r are the cooling and repump beam Rabi frequencies, determined by the relationship:

$$\Omega_c/\Gamma = \left(\frac{I_c}{39.8\text{mW cm}^{-2}}\right)^{\frac{1}{2}} \tag{4.19}$$

$$\Omega_r/\Gamma = \left(\frac{I_r}{39.0\text{mW cm}^{-2}}\right)^{\frac{1}{2}} \tag{4.20}$$

4.5 Frequency Comparison

Once the rf Paul trap was completely optimized with the lowest obtainable micromotion and secular motion, a frequency comparison with the endcap trap frequency was performed. Using the method described in Section 2.3, the center frequency of the clock transition beam was calculated for both traps, and then the frequency differences between the two traps was found for several different trials. Data of the AOM frequency offsets from the ULE cavity stabilized probe laser were collected by separate computer systems associated with each ion trap and later combined. The computers clocks were synchronized within 1 s of each other. Here we present the preliminary experimental results of this method.

A frequency scan of the clock transition with the 674 nm beam was done in order to identify the general positions of the Zeeman components. Since the traps had not been operated for an extended period of time, the center frequency of the ULE stabilized probe laser had drifted and it was difficult to assign the proper Zeeman components to the known theoretical relative frequency splitting and intensities. After a series of frequency scans, the correct Zeeman component assignments were made with respect to the approximate center frequencies as seen in figures 4.13 and 4.14. The Zeeman components relative intensities in the rf Paul trap scan are not as clearly defined as the endcap trap, but the positions were still identifiable. A number of spurious lines are observed in the rf Paul trap scans which are due to sidebands of the Zeeman components with the difference between two or

more secular oscillation frequencies. For example, the difference in the secular frequencies of the radial x and y directions are quite small and can be on the order of 10 kHz in magnitude. Combinations of the Zeeman transition frequency with this difference frequency can create numerous sidebands about each Zeeman component. Clear identification of the true Zeeman component from these sidebands was established by varying the rf Paul Trap ring symmetry voltage. This changes the secular frequencies and their differences but has no effect on the true Zeeman components. In this way, unambiguous identification of all Zeeman components was established.

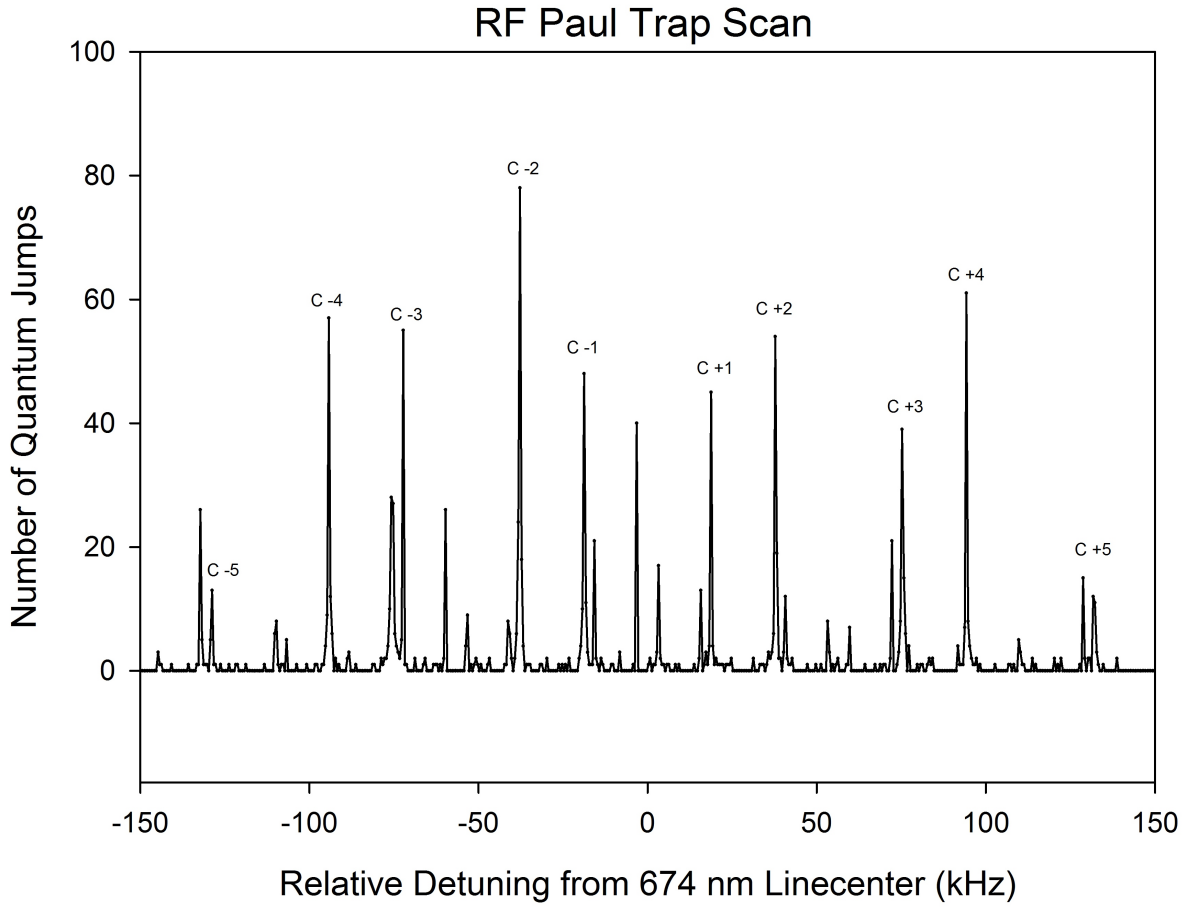

Figure 4.13: RF Paul Trap: Frequency scan of the 674 nm beam to identify Zeeman component locations.

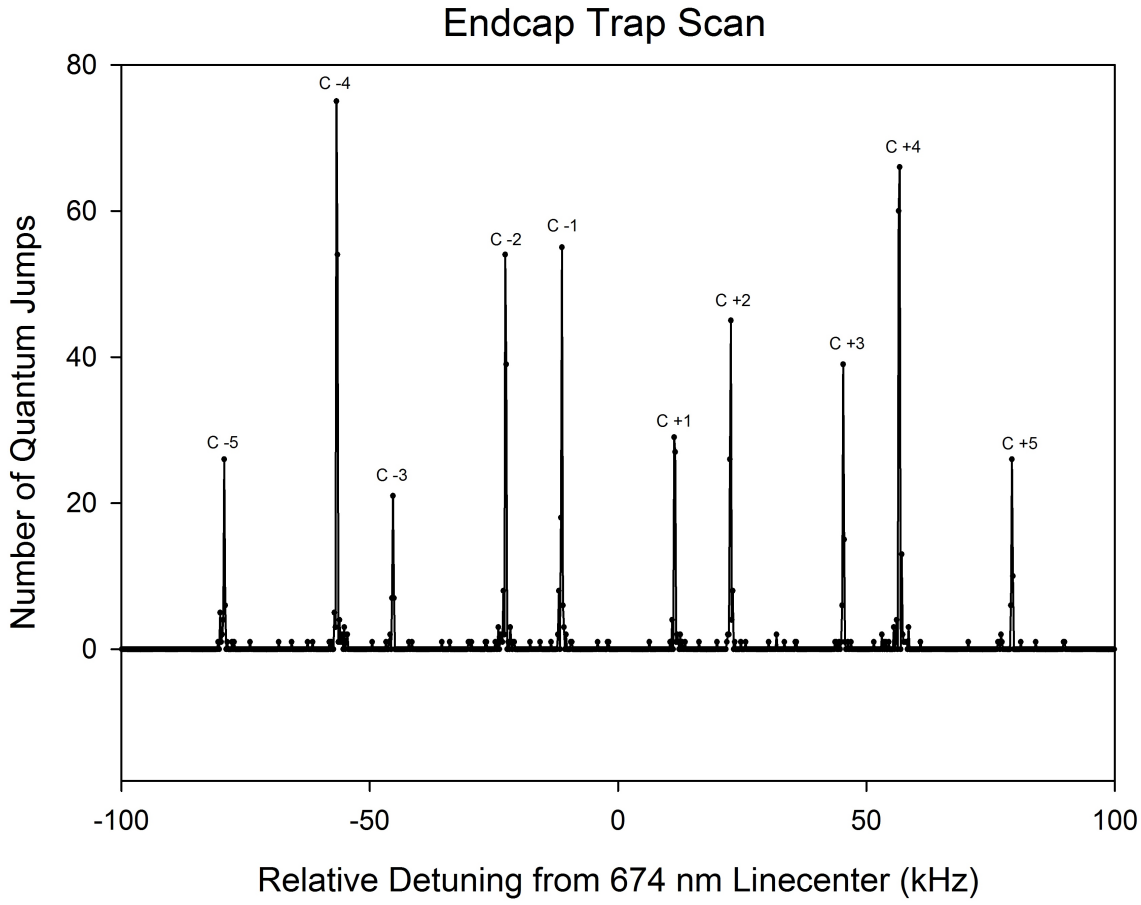

Figure 4.14: End Cap Trap: Frequency scan of the 674 nm beam to identify Zeeman component locations.

Once the Zeeman components were located, a locked centre frequency measurement of the clock transition was then performed. This lock run entails measuring the red and blue detuned half power points of the selected Zeeman component and determining the quantum jump transition rates at these points. The red and blue transition rates are then used to find a precise center frequency location for each Zeeman component. This is done for the red and blue Zeeman components of each Zeeman pair located on either side of the line centre, and then the precise Zeeman components pair centre frequencies are averaged to find the center frequency and Zeeman splitting of the 674 nm clock transition.

Figure 4.15 shows quantum jumps during a locked frequency run trial. Here only one Zeeman component data is shown for clarity. As can bee seen, the observed quantum jump rate is well removed from the origin and they can be used for the precise determination of the Zeeman component frequency. In these runs, the line centre is determined by using two Zeeman pairs of the $\pm C1$ and $\pm C2$ components.

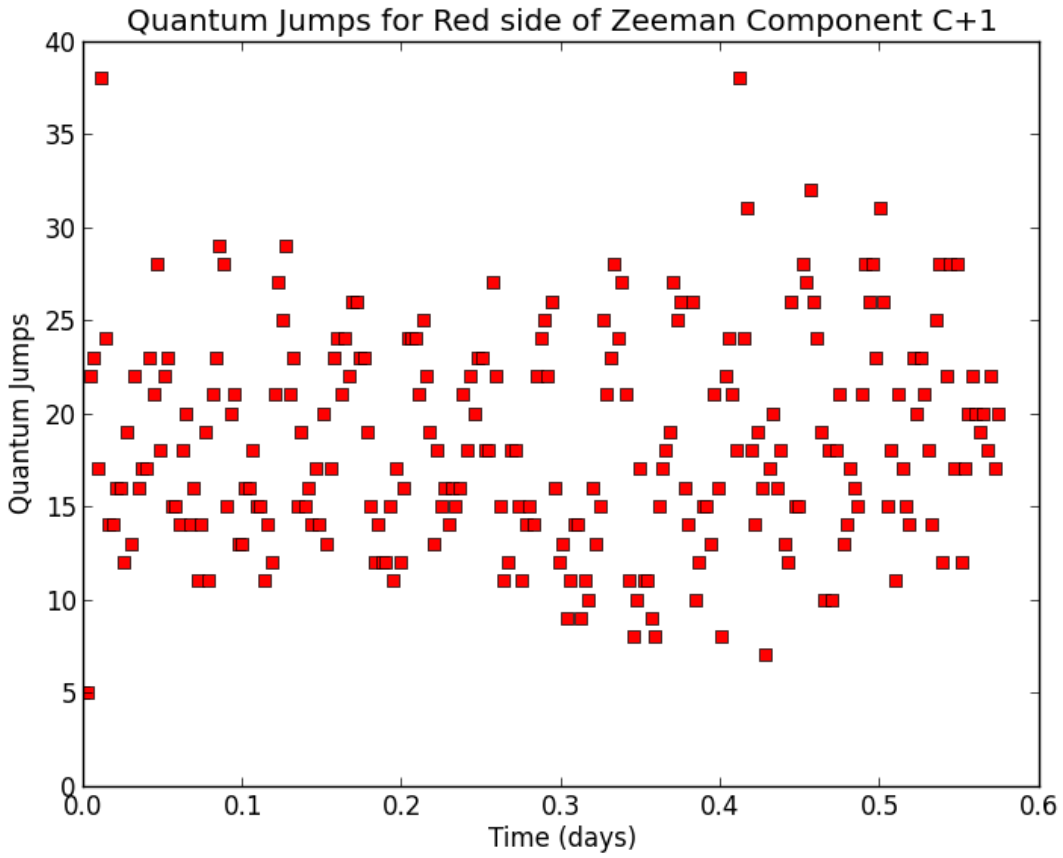

Figure 4.15: RF Paul trap: Number of quantum jumps for the red side of a Zeeman component (+C1).

The center frequencies of the clock transition were calculated during several simultaneous trials for the two ion traps. The frequency difference between the traps is found by subtracting the endcap trap frequency from the rf Paul trap frequency at the same times during the trials. Figure 4.16a shows the frequency difference of the traps during five trials in March 2013, the mean differences of each trial are shown with black squares and 1σ uncertainties. These uncertainties are determined from the standard deviation of averaged groups of data. The groups of data were selected to be averaged over an averaging time

which had the lowest Allan variance as described further in the text. The weighted mean of the March trials was -0.25 ± 0.09 Hz.

Another series of trials was performed in May 2013, seen in Figure 4.17a with a weighted mean of -1.14 ± 0.62 Hz. The last trial causes a significant increase in the trap mean frequency difference. This trial was performed after a series of unsuccessful attempts made over two hours to load an ion in the rf Paul trap at frequencies far from the trap 'magic' frequency. It is believed that this longer exposure to the loading oven flux created a larger level of uncompensated micromotion hence a larger shift. It is known that Sr metal deposition on the trap structure can cause the creation of patch potentials which further displace the ion from its ideal node in the trapping field [4]. This is likely the explanation for why the last trial has a much greater mean frequency difference almost making it an outlier, but still within the one standard deviation error of the other trials.

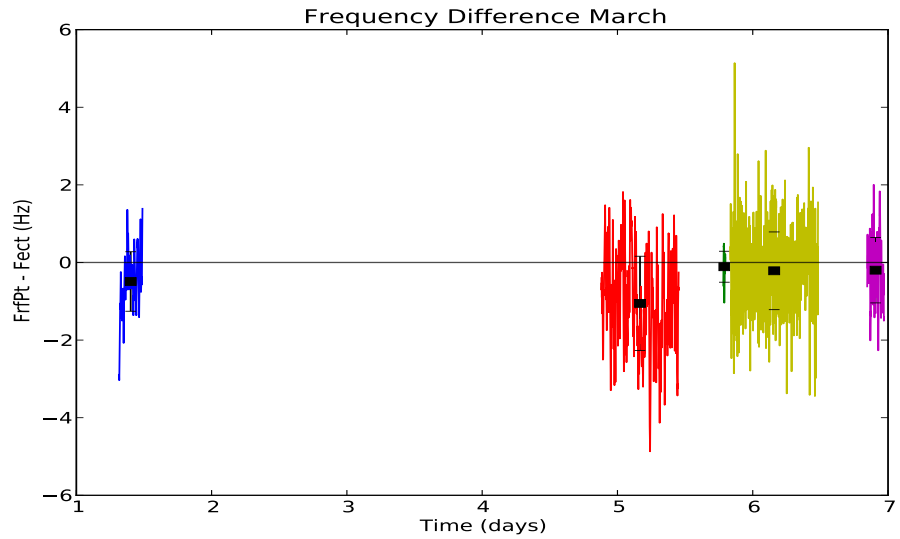

(a) Frequency Comparison: Trials comparing the frequency of the rf Paul trap with the endcap trap. The black squares are the mean frequency differences of each trial given with 1σ uncertainties. The weighted mean of these trials done in March 2013 was -0.25 $\pm$ 0.09 Hz.

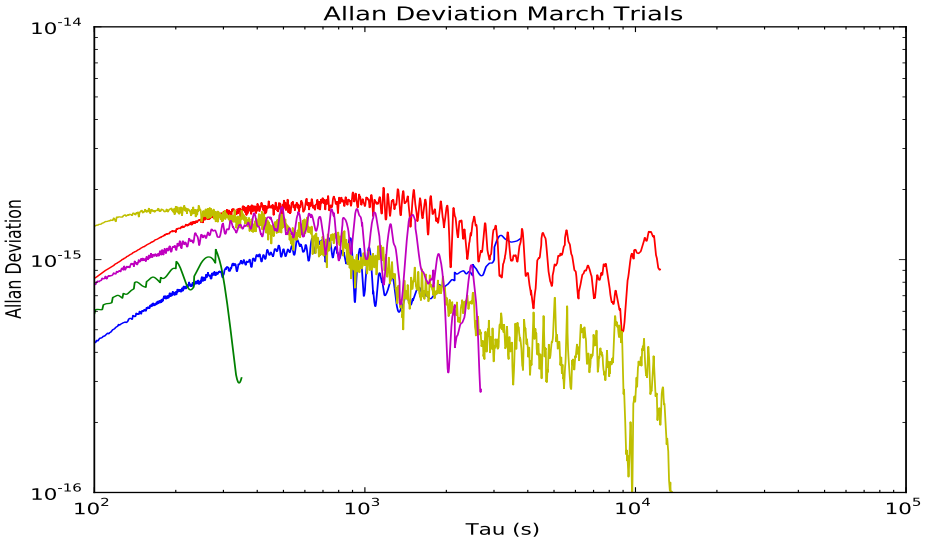

(b) Allan Deviations: A loglog plot of the Allan deviations of the ion traps' frequency difference as a function of measurement time. Colours correspond to the trials above.

Figure 4.16: Frequency comparison of the two ion traps with the associated Allan deviations of each trial executed in March 2013. The frequency difference was found by subtracting the center frequency of the endcap trap from the center frequency of the rf Paul trap.

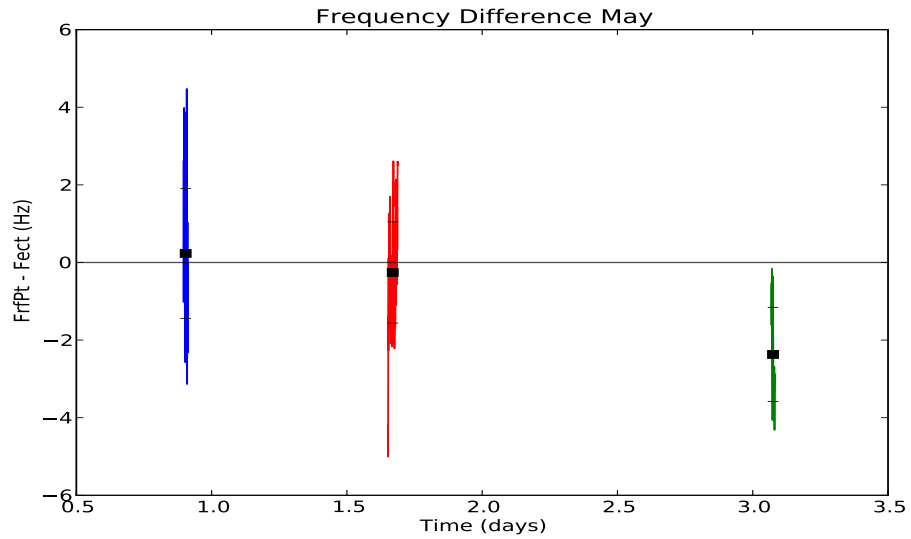

(a) Frequency Comparison: Trials comparing the frequency of the rf Paul trap with the endcap trap. The black squares are the mean frequency differences of each trial given with 1σ uncertainties. The weighted mean of these trials done in May 2013 was -1.14 $\pm$ 0.62 Hz.

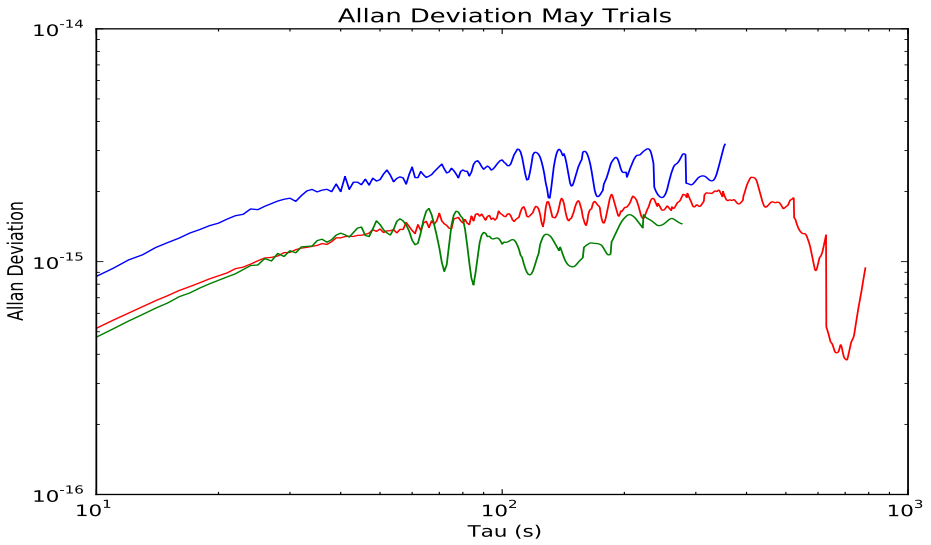

(b) Allan Deviations: A loglog plot of the Allan deviations of the ion traps' frequency difference as a function of measurement time. Colours correspond to the trials above.

Figure 4.17: Frequency comparison of the two ion traps with the associated Allan deviations of each trial executed in May 2013. The frequency difference was found by subtracting the center frequency of the endcap trap from the center frequency of the rf Paul trap.

In addition to the determination of the offset of the two ion trap systems, an effective evaluation of the frequency stability of the ion traps was performed. A parameter known as the Allan deviation provides a clear interpretation of the stability of a frequency standard. Briefly, Allan deviation is a measure of how much the deviation of a series of sequential data values have over different averaging times. It is based on the differences between adjacent measured frequency values, as opposed to the difference of each frequency value from the mean difference value. The following is a method used to calculate Allan deviations [47].

The instantaneous fractional frequency deviation is defined as:

$$y(t) = \frac{\Delta\nu(t)}{\nu_0} = \frac{dx(t)}{dt} \tag{4.21}$$

Where ν_0 is the frequency of the ideal oscillator, in this case the 444 779 044 095 485.3 Hz ion $S-D$ transition, and $\Delta\nu(t)$ is the change in frequency. The average fractional frequency deviation between two values can written:

$$\bar{y}_i(T_i, \tau) = \frac{x(T_i + \tau) - x(T_i)}{\tau} \tag{4.22}$$

where T is the length of measuring time and τ is the time between consecutive measurements. The Allan variance is expressed as:

$$\sigma_y^2(N, T, \tau) = \frac{1}{N-1} \sum_{i=1}^{N} \left(\bar{y}_i - \frac{1}{N} \sum_{j=1}^{N} \bar{y}_i \right)^2 \tag{4.23}$$

where N is the number of samples. The Allan deviation is simply the square root of the Allan variance:

$$\sigma_y = \sqrt{\sigma_y^2} \tag{4.24}$$

Figures 4.16b and 4.17b show the Allan deviations in loglog plots, allowing one to see possible trends over many different time scales. For averaging times shorter than 100 s the computer algorithm for stabilizing the AOM shifted frequency to the line centre has no effect due to the time constant of the routine being about 200 s. For these shorter time scales we observe basically the stability of the ULE cavity stabilized probe laser which is dominated by a drift for the time scale observed. Longer averaging times show the stability of the deviation at the 10^{-15} level with some runs showing improvement in stability with longer averaging times. Here, an Allan deviations on the order of 1×10^{-15} , gives an instability in frequency of about 0.4 Hz for the 445 THz clock transition.

Figure 4.18 is a compilation of the mean frequencies of all the trials performed in this work. The total weighted mean of all the ion trap frequency comparisons is -0.36 $\pm$ 0.08 Hz, which gives a fractional offset of about $8\times\ 10^{-16}$. This extremely small difference between two widely differing ion trap systems clearly illustrates the accurate and almost perfectly unperturbed environment in which the reference ion absorbers exist within. For reference, the best Cs atomic fountain realizations of the SI second worldwide are at the level of a few parts in 10^{-16} [10]. The rf Paul trap with its uncompensated micromotion approaches the performance of such standards. The results also clearly confirm that the strontium ion standard provides an extreme level of accuracy in its current state and can be further improved.

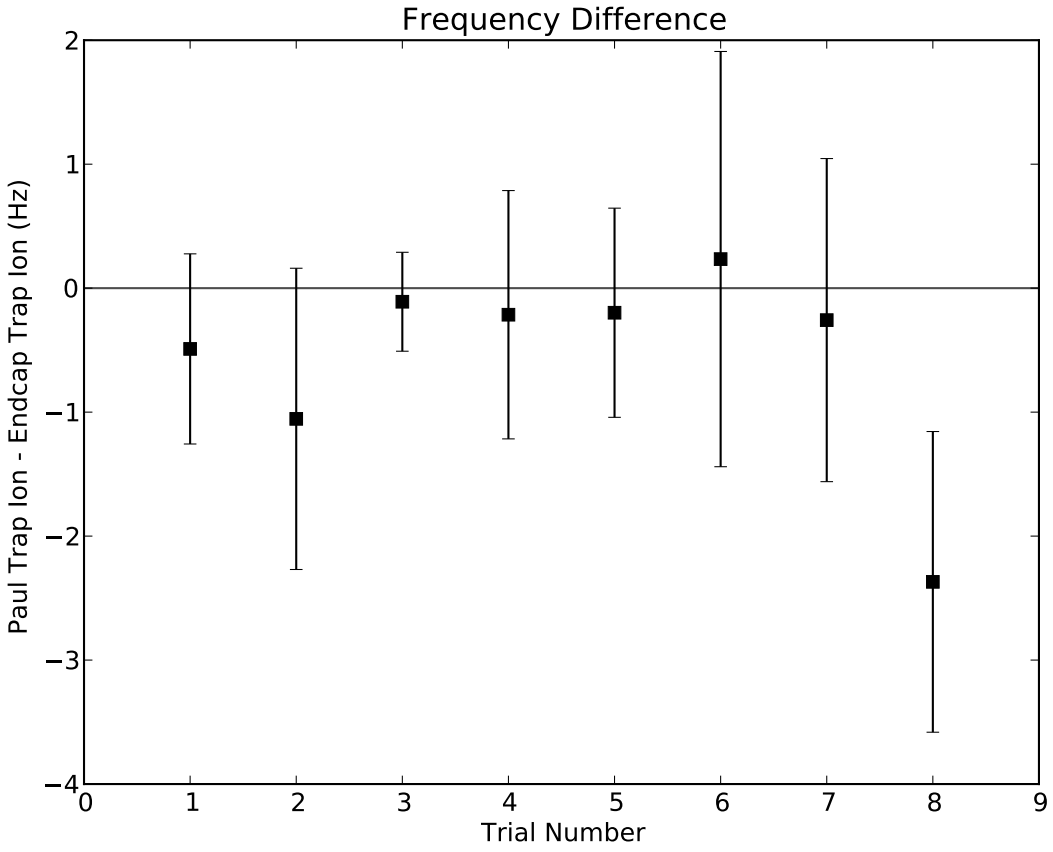

Figure 4.18: Overall Frequency Comparison: The mean frequency differences of the March and May 2013 trials given with 1σ uncertainties. The weighted mean of all the trials was -0.36±0.08 Hz.

4.5.1 Observed Frequency Difference with Trap Drive Frequency

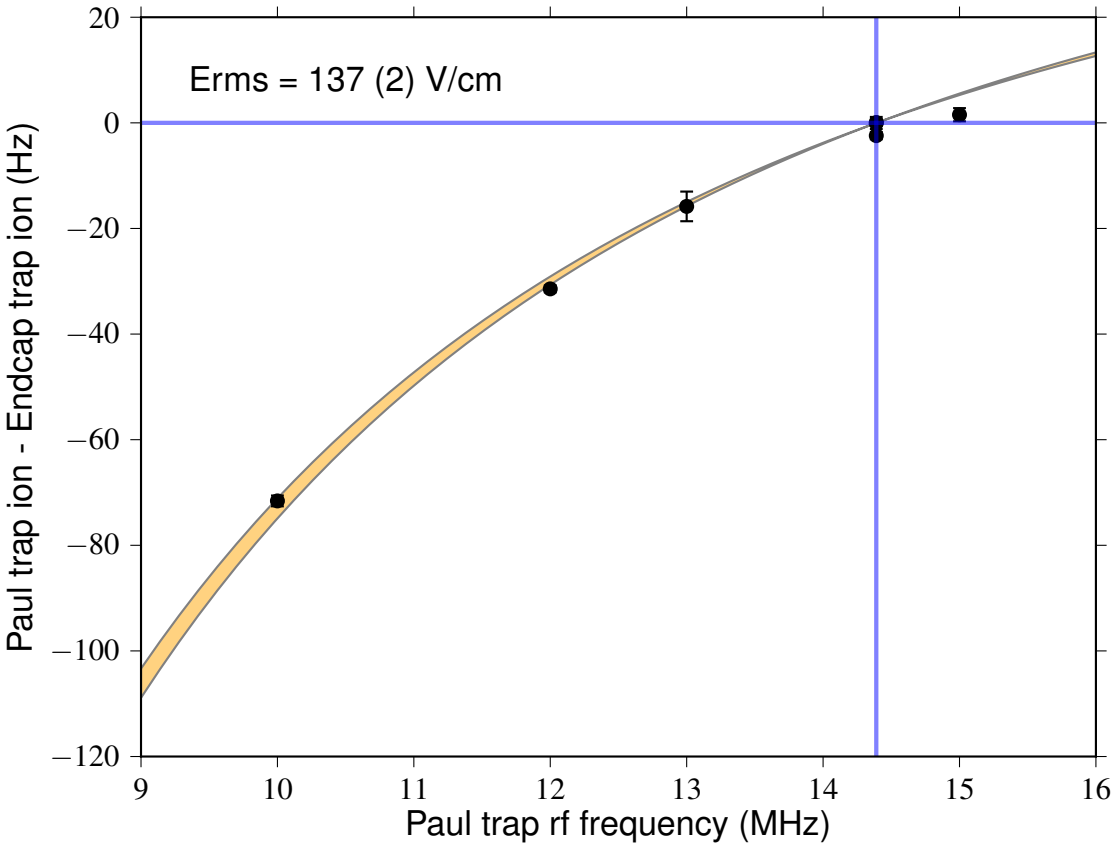

Figure 4.19: Frequency Comparison: The frequency differences of the rf Paul trap and Endcap trap with varying rf Paul trap frequency.

The trap comparison measurements were also used to investigate the level of micromotion isolation in the rf Paul trap by varying the trap drive frequency around the 'magic' frequency. Figure 4.19 is a plot of the ion traps' frequency difference for different rf Paul trap operational frequencies. Runs of approximately 2 hours in duration were taken with the rf trap tuned to different trap drive frequencies. The ion trap had to be reloaded and the axial micromotion minimized after every change in trap frequency. As can be seen, a clear and strong variation away from near zero occurs when the trap frequency is detuned from the ideal frequency of 14.39 MHz. Based on the discussion of the 'magic' frequency in the theory section and by combining expressions (2.10) and (4.7), the total micromotion induced frequency shift $\Delta\nu_\mu$ is related to the level of micromotion, atomic parameters, and

the trap drive frequency via:

$$\frac{\Delta\nu_\mu}{\nu_o} = -\frac{\langle E^2(t)\rangle}{2}\left[\left(\frac{e}{m\Omega c}\right)^2+\frac{\Delta\alpha_o}{h\nu_o}\right] \tag{4.25}$$

where $\langle E^2(t)\rangle$ is the mean squared electric field seen by the ion due to micromotion, e is the charge of the ion, m its mass, c the speed of light, Ω the trap drive frequency in angular units, $\Delta\alpha_o$ the difference in polarizability of the upper and lower states, h is Planck's constant and ν_o is the transition frequency. With the assumption that the level of micromotion is roughly constant over all the studies performed, a fit of the observed dependence with the above equation yields the solid curve shown in the figure. The calculation was performed using the best known value of the polarizability difference of $\Delta\alpha_o = -4.83(17) \times 10^{-40}$ J m^2/V^2 [3]. The fitted curve matches the observed data extremely well giving a root mean squared electric field of E_{rms} = 137 (2) V/cm. This value corresponds very well to estimates of the level of micromotion induced root mean square field performed on the rf Paul trap in 2005 of E_{rms} = 92 (14) V/cm [17]. This work provides the first direct confirmation of the cancellation of micromotion induced effects when the trap is operated at the 'magic' frequency and shows the utility of the method to isolate from micromotion effects and achieve high accuracy of the ion reference.

5 Conclusions

A high accuracy optical frequency comparison of the two optical clocks has been successfully completed. The $^{88}Sr^{+}$ ion $S-D$ clock transition in the older rf Paul trap system and the new endcap trap system were simultaneously observed and the fractional frequency difference was obtained. This was accomplished by modifying the rf Paul trap experimental system and operating the systems with optimal trapping, laser cooling, detection parameters so that each ion system's reference transition was observed with the lowest current level of perturbation. This included investigating ideal laser powers of the five radiations used in the rf Paul trap system, as well as replacing the Gaussian beam optics responsible for focussing the beams on the ion. These improvements resulted in achieving precision control of the beams and improved ion control in the trap environment in addition to increasing the reliability of factors contributing to holding the ion in the rf Paul trap for extended periods of time.

Various parameters pertaining to the trap environment were measured and calculated as a result of the studies performed in this work. The classical collisional rates were obtained for both the rf Paul trap and the endcap trap via mass spectroscopy. Hydrogen was the dominant gas species present, the total classical collisional rates of the rf Paul trap and end cap trap systems were $\gamma = 208 \times 10^{-4}\ s^{-1}$ and $\gamma = 52.6 \times 10^{-4}\ s^{-1}$ respectively. The higher collision rates observed in the rf Paul trap are consistent with the mean confinement lifetimes of the ions observed for the two trapping systems. The estimated clock transition fractional frequency shift due to the collisions is 8×10^{-18} for the rf trap and 2×10^{-18} for the endcap trap [3].

Studies of the level of observed micromotion were performed on the rf Paul trap along the sole direction of probing that was available. By performing precision spectroscopy of the Zeeman component and the micromotion sidebands, a field value of $E_{beam,rms} = 0.15$ V/cm along one minimized direction of beam propagation in the rf Paul trap was obtained. How-

ever, the total the root mean squared electric field, E_{rms}, is considered to be much larger and is considered the current main limitation on systematic uncertainties of the rf Paul trap apparatus. Later measurements based on the comparison of the two trap systems showed an estimated field value for the rf trap of E_{rms} = 137 (2) V/cm.

The ion temperature in the rf trap was calculated using the carrier-secular frequency sideband ratios, and the lowest optimized ion temperature obtained was 1.35 ± 0.38 mK. It was determined that an applied symmetry voltage and optimal cooling laser attenuation reduced the ion temperature. Power broadening was observed at different attenuations of the repump and cooling beams, determining a sharpest linewidth of the repump transition to be 57 MHz at the lowest sustainable intensity.

In recent work, the endcap trap Sr ion $S-D$ clock transition frequency was measured to be 444 779 044 095 485.5(9) Hz with a trap systematic shift uncertainty of 2.3×10^{-17} [3]. The rf Paul trap's fractional frequency uncertainty was estimated to be 3.4×10^{-14} in 2005 [17]. After a series of 8 frequency comparisons of the two traps, the total weighted mean of the trap frequency differences is 0.36 ± 0.08 Hz, which gives a fractional frequency difference of about 8×10^{-16}, demonstrating a major improvement of the rf trap uncertainty. This small offset between two very different trapping systems illustrates the accuracy of the $^{88}Sr^{+}$ ion traps as a frequency reference, and can continue to be greatly improved. The frequency difference obtained in these studies is comparable to the SI second realized with a Cs atomic fountain with a frequency uncertainty on the level of a few parts in 10^{-16} [10].

The improvement of the rf Paul trap system in this work will result in future studies where the rf trap will be used as a reference for more detailed systematic shift examinations of the endcap trap, which will one day assume the role of a contributor to international atomic frequency/time for Canada. Improvements to the endcap trap system can continue to be made with the aid of the rf Paul trap used as a stable reference, including a more detailed analysis of the value for the difference in the polarizabilites of the $D_{5/2}$ and $S_{1/2}$ $^{88}Sr^{+}$ ion levels, $\Delta\alpha_o$, using the method seen in Figure 4.19. Finally, the results of this work will contribute to sensitive measurements of General Relativity. By raising the relative height of the rf Paul trap to the endcap trap from Earth's surface by only a meter, the level of accuracy of these optical clocks will sense the change in local time in the Earth's field of about 10^{-16} m^{-1}. A similar experiment to this was performed at NIST in 2010, where two Al^{+} optical clocks frequency differences where measured at height differences of 17 cm and 33 cm. A fractional frequency change of 4.1±1.6 $\times 10^{-17}$ was obtained for these two

measurements [48].

The goal of this work was successfully achieved and the results produced an observed frequency difference between optical clock reference systems comparable to the current world-wide results reported. These overall improvements of frequency and time standards benefit any application involving measurements depending on precision frequency. These include tests of fundamental physics and cosmology theories, metrology, global navigation satellite systems, gravitational wave detection, and relativity.

References

[1] A.A. Madej and J.E. Bernard. Single-ion optical frequency standards and measurements of their absolute optical frequency. *Frequency Measurements and Control: Topics in Applied Physics*, 79:153–194, 2001.

[2] G. Kamas. *Time and Frequency Users's Manual*. National Bureau of Standards, 1977. National Bureau of Standards Technical Note 695.

[3] P. Dubé, A.A. Madej, Z. Zhou, and J. Bernard. Evaluation of systematic shifts of the $^{88}Sr^{+}$ single-ion optical frequency standard at the 10^{-17} level. *Physical Review A*, 87:023806, 2013.

[4] M. Brownnutt, V. Letchumanan, G. Wilpers, R.C. Thompson, P. Gill, and A.G. Sinclair. Controlled photoionization loading of $^{88}Sr^{+}$ for precision ion-trap experiments. *Applied Physics B*, 87:411–415, May 2007.

[5] A.A. Madej and J.D. Sankey. Quantum jumps and the single trapped barium ion: Determination of collisional quenching rates for the $5d\,^2D_{5/2}$ level. *Physical Review A*, 41(5):2621–2630, 1990.

[6] A.D. Shiner, A.A. Madej, P. Dubé, and J.E. Bernard. Absolute optical frequency measurement of saturated absorption lines in Rb near 422 nm. *Appl. Phys. B*, 89(4):595–601, 2007.

[7] P. Dubé, A.A. Madej, J. Bernard, J.E Bernard, and A.D. Shiner. A narrow linewidth and frequency-stable probe laser source for the $^{88}Sr^{+}$ single ion optical frequency standard. *Applied Physics B*, 95(1):43–54, 2009.

[8] National Institute of Standards and Technology. *The International System of Units (SI)*, NIST special publication 330 edition, 2008.

[9] T. Rosenband, D. B. Hume, P. O. Schmidt, C. W. Chou, L. Brusch, A. Lorini, W. H. Oskay, R. E. Drullinger, T. M. Fortier, J. E. Stalnaker, S. A. Diddams, W. C. Swann, N. R. Newbury, W. M. Itano, D. J. Wineland, and J. C. Bergquist. Frequency ratio of Al^+ and Hg^+ single-ion optical clocks; metrology at the 17th decimal place. *Science*, 319:1808–1812, March 2008.

[10] S. Weyers, V. Gerginov, N. Nemitz, R. Li, and K. Gibble. Distributed cavity phase frequency shifts of the caesium fountain PTB-CSF2. *Metrologia*, 49(1):82, 2012.

[11] A.A. Madej, J.E. Bernard, P. Dubé, and L. Marmet. Absolute frequency of the $^{88}Sr^+$ $5s\ ^2S_{1/2} - 4d\ ^2D_{5/2}$ reference transition at 445 THz and evaluation of systematic shifts. *Physical Review A*, 70:012057, 2004.

[12] Th. Udem, S. A. Diddams, K. R. Vogel, C. W. Oates, E. A. Curtis, W. D. Lee, W. M. Itano, R. E. Drullinger, J. C. Bergquist, and L. Hollberg. Absolute frequency measurements of the Hg^+ and Ca optical clock transitions with a femtosecond laser. *Physical Review Letters*, 86:4996–4999, May 2001.

[13] J. v. Zanthier, Th. Becker, M Eichenseer, A. Yu. Nevsky, E. Schwedes, Ch.and Peik, R. Holzwarth, J. Reichert, Th. Udem, Th. Hänsch, P.V. Pokasov, M.N. Skvortsov, and S.N. Bagayev. Absolute frequency measurement of the In^+ clock transition with a mode-locked laser. *Optics Letters*, 25:1729–1731, 2000 2000.

[14] J. Stenger, C. Tamm, N. Haverkamp, S. Weyers, and H. Telle. Absolute frequency measurement of the 435.5-nm $^{171}Yb^+$clock transition with a kerr-lens mode-locked femtosecond laser. *Optics Letters*, 26:1589–1591, 2001.

[15] C.W. Chou, D.B. Hume, J.C.J. Koelemeij, D.J. Wineland, and T. Rosenband. Frequency comparison of two high-accuracy Al^+ optical clocks. *Physical Review Letters*, 104(7):070802–4, 2010.

[16] C.A. Schrama, E. Peik, W.W. Smith, and H. Walther. Novel miniature ion traps. *Optics Communications*, 101:32–36, 1993.

[17] P. Dubé, A. A. Madej, J. E. Bernard, L. Marmet, J.-S. Boulanger, and S. Cundy. Electric quadrupole shift cancellation in single-ion optical frequency standards. *Phys. Rev. Lett.*, 95:033001, Jul 2005.

[18] G.P. Barwood, G. Huang, H.A. Klein, and P. Gill. Subkilohertz comparison of the

single-ion optical-clock $^2S_{1/2}-^2D_{5/2}$ in two $^{88}Sr^+$ traps. *Physical Review A*, 59(5):3178–4, 1999.

[19] G.P. Barwood, P. Gill, G. Huang, and H.A. Klein. Characterization of a $^{88}Sr^+$ optical frequency standard at 445 THz by two-trap comparison. In *Proceedings of the 2012 IEEE International Frequency Control Symposium, Baltimore, Maryland, USA , 21-24 May 2012*, pages 270–271, 2012.

[20] R. H. Dicke. The effect of collisions upon the doppler width of spectral lines. *Phys. Rev.*, 89:472–473, Jan 1953.

[21] W. Neuhauser, M. Hohenstatt, P. Toschek, and H. Dehmelt. Optical-sideband cooling of visible atom cloud confined in parabolic well. *Phys. Rev. Lett.*, 41:233–236, Jul 1978.

[22] W. Jones. Earnshaw's theorem and the stability of matter. *European Journal of Physics*, 1(2):85, 1980.

[23] R. Blatt, P. Gill, and R.C. Thompson. Current perspectives on the physics of trapped ions. *Journal of Modern Optics*, 39(2):193–220, 1992.

[24] R.E. March. An introduction to quadrupole ion trap mass spectrometry. *Journal of Mass Spectrometry*, 32(4):351–369, 1997.

[25] R.F. Wuerker, H. Shelton, and R.V. Langmuir. Electrodynamic containment of charged particles. *Journal of Applied Physics*, 30(3):342–349, 1958.

[26] S. Urabe, M. Watanabe, H. Imajo, K. Hayasaka, U. Tanaka, and R. Ohmukai. Observation of doppler sidebands of a laser-cooled Ca^+ ion by using a low-temperature-operated laser diode. *Applied Physics B*, 67(2):223–227, 1998.

[27] J.D. Sankey and A.A. Madej. The production of ions for single-ion traps. *Applied Physics B*, 49(1):69–72, 1989.

[28] S. Gulde, D. Rotter, P. Barton, F. Schmidt-Kaler, R. Blatt, and W. Hogervorst. Simple and efficient photo-ionization loading of ions for precision ion-trapping experiments. *Applied Physics B*, 73:861–863, 2001.

[29] A. Gallagher. Oscillator strengths of Ca II, Sr II, and Ba II. *Physical Review*, 157(1):24–30, 1966.

[30] H.G. Dehmelt. Mono-ion oscillator as potential ultimate laser frequency standard. *IEEE Transactions on Instrumentation and Measurement*, 31(2):83–87, 1982.

[31] D. J. Wineland, W. M. Itano, J. C. Bergquist, and R. G. Hulet. Laser-cooling limits and single-ion spectroscopy. *Phys. Rev. A*, 36:2220–2232, Sep 1987.

[32] V. Letchumanan, M.A. Wilson, P. Gill, and A.G. Sinclair. Lifetime measurement of the metastable $4d\ ^2D_{5/2}$ state in $^{88}Sr^+$ using a single trapped ion. *Physical Review A*, 72:012509, 2005.

[33] Andrew Shiner. Development of a frequency stabilized 422 nm diode laser system and its application to a $^{88}Sr^+$ single ion optical frequency standard. Master's thesis, York University, 2006.

[34] J. E. Bernard, L. Marmet, and A. A. Madej. A laser frequency lock referenced to a single trapped ion. *Optics Communications*, 150:170–174, 1998.

[35] D. J. Berkeland, J. D. Miller, J. C. Bergquist, W. M. Itano, and D. J. Wineland. Minimization of ion micromotion in a paul trap. *Journal of Applied Physics*, 83(10):5025–5033, 1998.

[36] D. Jiang, B. Arora, M.S. Safronova, and C.W. Clark. Blackbody-radiation shift in a $^{88}Sr^+$ ion optical frequency standard. *Journal of Physics B: Atomic, Molecular and Optical Physics*, 42:154020–154026, 2009.

[37] T.W. Hänsch and B. Couillaud. Laser frequency stabilization by polarization spectroscopy of a reflecting reference cavity. *Optics Communications*, 35(3):441 – 44, 1980.

[38] M. Vainio, J.E. Bernard, and L. Marmet. Cavity-enhanced optical frequency doubler based on transmission-mode Hänsch - Couillaud locking. *Applied Physics B*, 104(4):897–908, 2011.

[39] Gideon Humphrey. Frequency stabilization of a 1092 nm diode-pumped fiber laser and a 1033 nm external cavity diode laser for use in an optical atomic clock based on a $^{88}Sr^+$ single ion. Master's thesis, York University, 2009.

[40] R.W.P. Drever, J.L. Hall, F.V. Kowalski, J. Hough, G.M. Ford, A.J. Munley, and H. Ward. Laser phase and frequency stabilization using an optical resonator. *Applied Physics B*, 31(2):97–105, 1983.

[41] Ifan Hughes. *Gaussian Beams and the Knife-Edge Measurement*. Durham University, 2006.

[42] A.E. Siegman. *An Introduction to Lasers and Masers*, chapter Optical Resonators and Lens Waveguides, pages 312–313. McGraw-Hill Inc., 1979.

[43] A. A. Madej and J. D. Sankey. Single, trapped Sr^+ atom: laser cooling and quantum jumps by means of the 4d $^2D_{5/2}$–5s $^2S_{1/2}$ transition. *Opt. Lett.*, 15(11):634–635, Jun 1990.

[44] T. Su. *Gas Phase ion Chemistry: Classical ion-molecule collision theory*, volume 1, chapter 3, pages 83–117. Academic Press, 1979.

[45] T. Lindvall, M. Merimaa, I. Tittonen, and A.A. Madej. Dark-state suppression and optimization of laser cooling and fluorescence in a trapped alkaline-earth-metal single ion. *Physical Review A*, 86:033403, 2012.

[46] J. Javanainen. Light pressure cooling of trapped ions in three dimensions. *Applied Physics B*, 23(2):175–182, 1980.

[47] F. Riehle. *Frequency Standards Basics and Applications*. Wiley-Vch, 2004.

[48] C.W. Chou, D.B. Hume, T. Rosenband, and D.J. Wineland. Optical clocks and relativity. *Science*, 329:1630–1633, 2010.